Department of Applied Physics

Studies on Wettability

From Fundamental Concepts and Nanofibrous Materials to Applications

Juuso T. Korhonen

Aalto University

DOCTORAL DISSERTATIONS

Aalto University publication series
DOCTORAL DISSERTATIONS 116/2013

Studies on Wettability

From Fundamental Concepts and Nanofibrous Materials to Applications

Juuso T. Korhonen

Doctoral dissertation completed for the degree of Doctor of Science in Technology to be presented with due permission of the School of Science for public examination and debate in Auditorium AS1 at the Aalto University School of Science (Espoo, Finland) on the 9th August 2013 at 12 noon.

Aalto University
School of Science
Department of Applied Physics
Molecular Materials & Soft Matter and Wetting

Supervising professor
Acad. Prof. Olli Ikkala

Thesis advisors
Acad. Prof. Olli Ikkala
Dr. Robin Ras

Preliminary examiners
Prof. Jurkka Kuusipalo, Tampereen teknillinen yliopisto
Dr. Ilker S. Bayer, Istituto di Tecnologia (IIT), Italy

Opponent
Prof. Gareth McKinley, Massachusetts Institute of Technology, U.S.A.

Aalto University publication series
DOCTORAL DISSERTATIONS 116/2013

ISBN 978-952-60-5259-5 (printed)
ISBN 978-952-60-5260-1 (pdf)
ISSN-L 1799-4934
ISSN 1799-4934 (printed)
ISSN 1799-4942 (pdf)
http://urn.fi/URN:ISBN:978-952-60-5260-1

http://lib.tkk.fi/Diss/

Unigrafia Oy
Helsinki 2013

Finland

441 697
Printed matter

Aalto University

Abstract

Aalto University, P.O. Box 11000, FI-00076 Aalto www.aalto.fi

Author
Juuso T. Korhonen

Name of the doctoral dissertation
Studies on Wettability: From Fundamental Concepts and Nanofibrous Materials to Applications

Publisher School of Science

Unit Department of Applied Physics

Series Aalto University publication series DOCTORAL DISSERTATIONS 116/2013

Field of research Engineering Physics, Physics

Manuscript submitted 11 June 2013 **Date of the defence** 9 August 2013

Permission to publish granted (date) 27 June 2013 **Language** English

☐ **Monograph** ☒ **Article dissertation (summary + original articles)**

Abstract

Water is among the most vital substances on earth. Despite being an everyday element, prominently interesting phenomena occur when water is in contact with a surface. Superhydrophobic surfaces are ones that do not wet. In the extreme, they repel water to such a large degree that water does not stick to even nearly horizontal planes. Nowadays, many researchers pursue the magnificent examples set by nature, such as the extraordinary water repellency of a lotus leaf. Even though the basis of the study of wetting dates back to the 1800s, many elementary concepts remain unexplored. This thesis combines fundamental notions of wetting to experimental material science and demonstrates applications based on these materials, ranging from memory devices and sensors to pellets, which facilitate environmental clean-up.

Publication I studies the fundamental concepts of surface wetting characterization and introduces a quantitative method for measuring the receding contact angle using the sessile-drop method. Theory and experiments together with calculations evaluate the validity of the developed model, and good agreement between theory and experiments is found. Furthermore, a novel definition for superhydrophobicity is proposed.

Publication II introduces a growth model for the synthesis of silicone nanofilaments, which are one-dimensional nanostructures used to create superhydrophobic surfaces. In contrast to the previous studies, the present model explains the break of symmetry occurring in the initial phase of the growth, which has so far been implicitly assumed.

Publication III demonstrates a hierarchically rough surface, which exhibits bi-stable superhydrophobic wetting states under water. A rapid local wetting transition occurs simply by locally applying pressure or suction onto the surface. Theoretical considerations explain the phenomena and a simple display demonstrates the concept.

Publications IV and **V** introduce nanocellulose aerogels coated by atomic layer deposition with inorganic thin films. These materials are further employed as a resistive/capacitive humidity sensor and for oil spill cleanup from a water surface. The porosity and high surface area of the structures together with the wetting properties of the inorganic coating account for the observed properties. In addition, the study evaluates different drying methods for the nanocellulose aerogels based on the aggregation of the fibrils.

Combining basic principles of wetting and superhydrophobicity to novel materials, as shown in this study, can lead to applications from myriad fields of technology. The concepts and applications demonstrated hopefully inspire future research towards many wetting-based applications.

Keywords wetting, superhydrophobicity, nanocellulose, aerogel, humidity sensor, oil absorption

ISBN (printed) 978-952-60-5259-5 **ISBN (pdf)** 978-952-60-5260-1

ISSN-L 1799-4934 **ISSN (printed)** 1799-4934 **ISSN (pdf)** 1799-4942

Location of publisher Espoo **Location of printing** Helsinki **Year** 2013

Pages 136 **urn** http://urn.fi/URN:ISBN:978-952-60-5260-1

A! Aalto-yliopisto

Tiivistelmä

Aalto-yliopisto, PL 11000, 00076 Aalto www.aalto.fi

Tekijä
Juuso T. Korhonen

Väitöskirjan nimi
Kastuvuustutkimuksia: Peruskäsitteistä ja kuitumaisista nanorakenteista sovelluksiin

Julkaisija Perustieteiden korkeakoulu

Yksikkö Teknillisen fysiikan laitos

Sarja Aalto University publication series DOCTORAL DISSERTATIONS 116/2013

Tutkimusala Teknillinen fysiikka, fysiikka

Käsikirjoituksen pvm 11.06.2013 **Väitöspäivä** 09.08.2013

Julkaisuluvan myöntämispäivä 27.06.2013 **Kieli** Englanti

☐ **Monografia** ☒ **Yhdistelmäväitöskirja (yhteenveto-osa + erillisartikkelit)**

Tiivistelmä

Vesi on arkipäiväinen, mutta elintärkeä aine. Veden kastelemilla pinnoilla tapahtuu erittäin mielenkiintoisia ilmiöitä. Superhydrofoobiset pinnat ovat sellaisia, joilta pisarat vierivät pois vaikka pinta olisi lähes vaakasuorassa. Nykyään monet tutkijat pyrkivät jäljittelemään luonnossa esiintyviä ilmiöitä ja rakenteita, kuten esimerkiksi lootuskukan lehden äärimmäistä vedenhylkimiskykyä. Vaikka pintojen kastuvuustutkimuksen perusta luotiin jo 1800-luvun alussa, monia perustavanlaatuisia käsitteitä on edelleen tutkimatta. Tämä työ yhdistää teoreettisia konsepteja kokeelliseen materiaalitieteeseen ja esittelee näille uusille materiaaleille sovelluksia digitaalisista muisteista öljyntorjuntapelletteihin.

Julkaisu I tutkii pintojen kastuvuuden peruskäsitteitä ja esittää kvantitatiivisen kokeellisen menetelmän, jolla voidaan mitata pinnan vetäytyvän kontaktikulman arvo käyttämällä ns. pisaramenetelmää. Vastaavuus teorettisen konseptin, laskennallisten mallin sekä kokeiden välillä todennetaan. Lisäksi työssä ehdotetaan uutta määritelmää superhydrofoobisuudelle.

Julkaisu II esittelee kasvumallin, joka selittää kuinka silikoninanofilamentit, jotka ovat superhydrofoobisia kuitumaisia nanorakenteita, kasvavat pinnoille. Aiemmissa malleissa ei olla pystytty täysin kuvaamaan kuinka tetragonaalisista lähtöaineista muodostuu yksiulotteisia rakenteita. Ehdotettu malli pyrkii kattamaan juuri tämän symmetrian rikkoutumisen.

Julkaisu III käsittelee hierarkkista pintaa, jolla esiintyy kaksi superhydrofoobista kastumistilaa, kun se asetetaan veden alle. Paikalliset painemuutokset aiheuttavat nopean ja paikallisen muutoksen tilasta toiseen. Teoria ja kokeet osoittavat, että molemmat tilat ovat pitkäikäisiä ja konseptia havainnollistetaan käyttämällä pintaa yksinkertaisena näyttölaitteena.

Julkaisut IV ja **V** kuvailevat nanoselluloosa-aerogeelejä, jotka on pinnoitettu epäorgaanisilla aineilla käyttäen atomikerroskasvatusmenetelmää, ja joiden avulla voidaan luoda sekä resistiivinen/kapasitiivinen kosteusanturi että pelletti, jota voidaan käyttää öljylauttojen imeyttämiseen suoraan veden pinnalta. Aerogeelien suuri huokoisuus ja suuri pinta-ala mahdollistavat esitellyt ominaisuudet. Lisäksi työssä vertaillaan erilaisia nanoselluloosa-aerogeelien kuivausmenetelmiä kuitumaisen verkostorakenteen säätämiseksi.

Kastuvuusilmiöiden peruskäsitteiden yhdistäminen materiaalitieteeseen, kuten tässä työssä on tehty, voi johtaa mielenkiintoisiin sovelluksiin monella tekniikan alalla. Esitellyt konseptit ja sovellukset toivottavasti inspiroivat jatkotukimuksia, joissa yhdistellään kastuvuusilmiöitä sovelluksiin.

Avainsanat kastumisilmiöt, superhydrofoobisuus, nanoselluloosa, aerogeeli, kosteusanturi, öljyn imeytys

ISBN (painettu) 978-952-60-5259-5 **ISBN (pdf)** 978-952-60-5260-1

ISSN-L 1799-4934 **ISSN (painettu)** 1799-4934 **ISSN (pdf)** 1799-4942

Julkaisupaikka Espoo **Painopaikka** Helsinki **Vuosi** 2013

Sivumäärä 136 **urn** http://urn.fi/URN:ISBN:978-952-60-5260-1

Preface

Ten years ago, I started as an undergraduate student at the department of Engineering Physics and Mathematics in Helsinki University of Technology with a goal of becoming a physicist. It was clear to me from the beginning that to be a physicist is to be a doctor and a master's degree would not suffice. Therefore, I was extremely satisfied in 2005 when Prof. Olli Ikkala took me as a summer trainee into his laboratory, which was at the time was known as the Polymer Physics group. I graduated as a Master of Science in 2007 and I started as a graduate student in early 2008. I'm extremely grateful to Prof. Olli Ikkala for providing me this opportunity to work in such a versatile, inspiring, and ambitious environment.

My research path has not been exactly straightforward. I started in the field of supramolecular chemistry and block copolymer self-assembly, which introduced me to the basics of material characterization and even to some elementary chemistry. However, I was promptly directed towards atomic layer deposition and nanocellulose. Afterwards, my research focus was directed more and more towards wettability and superhydrophobicity, which was made possible by Dr. Robin Ras, to whom I am indebted for introducing me to this incredibly fascinating field.

Moreover, I thank Prof. Janne Ruokolainen for the opportunity to work with electron microscopy and especially the scanning electron microscopes at the Nanomicroscopy Center. Through the collaborations we did and all the interaction with the users, my knowledge of both scientific instruments and human behavior has expanded.

I am grateful for the successful collaboration we conducted with Jari Malm and Prof. Maarit Karppinen from the Laboratory of Inorganic Chemistry. Tuukka Verho deserves a special mention for introducing me to world of silicone nanofilaments and wetting theory. Working together with Tommi Huhtamäki has been fruitful and I thank him for all the good data he has provided. I also

express my sincere gratitude to all other collaborators — both successful and unsuccessful — for it is through trial and error, that we learn.

At times, I perhaps did not believe that I would ever become a doctor, yet now this goal is actually becoming a reality. One of the most positive influential factors in the process was the open and diverse working community at the group. We have been able to share our joys, sorrows, and frustrations with each other. First, I collectively thank everyone in the group for keeping up the warm atmosphere. A special mention goes to Susanna Junnila, with whom I shared an office for seven years. It is needless to say that we helped each other out in every turn. I would also like to state my gratitude to Jaana Vapaavuori whose attitude towards life I admire. Panu Hiekkataipale deserves a special thanks for helping me out numerous times. However, it is not all work and no play... we also have enjoyed weekly jogging trips, frisbee games, climbing, sauna, and of course the traditional summer, pre-xmas, and vappu parties.

I thank Prof. Jurkka Kuusipalo from Tampere University of Techonology and Dr. Ilker Bayer from Italian Institute of Technology for the preliminary examination of the thesis. I thank Prof. Gareth McKinley from Massachusetts Institute of Technology already in advance for accepting to act as the opponent at the dissertation.

Hard work needs to be balanced by relaxing free-time and activities. In reality, without the experiences together with my band mates, climbing buddies, and other friends, this achievement would not have been possible. I express my deepest gratitude to all of you. I special mention goes out to Maria; you are my family, but you are also my friend.

Lopulta tärkein asia elämässäni on perhe. Olen loputtoman kiitollinen vanhemmilleni upeasta kasvatuksesta ja tuesta, jonka ansiosta olen kasvanut täksi ihmiseksi, joka olen. Kiitos!

Kiitos Tuuli ehtymättömästä ymmärryksestäsi ja tuestasi!

Oiva ja Selma olette elämäni valo.

Espoo, Finland, July 8, 2013,

Juuso T. Korhonen

Contents

List of Publications

This thesis consists of an overview and of the following publications which are referred to in the text by their Roman numerals.

I J. T. KORHONEN, T. HUHTAMÄKI, O. IKKALA, and R. H. A. RAS
Reliable Measurement of the Receding Contact Angle.
Langmuir, 29, 3858–3863, 2013.

II J. T. KORHONEN, T. HUHTAMÄKI, and R. H. A. RAS
Growth Model for Hollow Silicone Nanofilaments Based on Local Pressure-Induced Film Expansion.
Submitted, June 2013.

III T. VERHO, J. T. KORHONEN, L. SAINIEMI, V. JOKINEN, C. BOWER, K. FRANZE, S. FRANSSILA, P. ANDREW, O. IKKALA, and R. H. A. RAS
Reversible Switching Between Superhydrophobic States on a Hierarchically Structured Surface.
Proceedings of the National Academy of Sciences of the United States of America, 109, 10210–10213, 2012.

IV J. T. KORHONEN, P. HIEKKATAIPALE, J. MALM, M. KARPPINEN, O. IKKALA, and R. H. A. RAS
Inorganic Hollow Nanotube Aerogels by Atomic Layer Deposition onto Native Nanocellulose Templates.
ACS Nano, 5, 1967–1974, 2011.

V J. T. KORHONEN, M. KETTUNEN, R. H. A. RAS, and O. IKKALA
Hydrophobic Nanocellulose Aerogels as Floating, Sustainable, Reusable, and Recyclable Oil Absorbents.
ACS Applied Materials & Interfaces, 3, 1813–1816, 2011.

Author's Contribution

Publication I: "Reliable Measurement of the Receding Contact Angle"

The author designed and performed the experiments together with B.Sc. Tommi Huhtamäki, analyzed the data, derived the theory, performed numerical calculations, and wrote the manuscript.

Publication II: "Growth Model for Hollow Silicone Nanofilaments Based on Local Pressure-Induced Film Expansion"

The author designed the concept, planned and performed the experiments with B.Sc. Tommi Huhtamäki, analyzed the data, developed the theory, and wrote the manuscript.

Publication III: "Reversible Switching Between Superhydrophobic States on a Hierarchically Structured Surface"

The author participated in performing the experiments, and analyzing the data together with M.Sc. Tuukka Verho. Microfabrication and confocal microscopy were performed by collaborators. The author commented on several of the revisions of the manuscript and proof-read the theory.

Publication IV: "Inorganic Hollow Nanotube Aerogels by Atomic Layer Deposition onto Native Nanocellulose Templates"

The author took part in designing the concept, designed and performed the experiments, and analyzed the data. The author wrote the first draft of the

manuscript and edited the revisions based on the input from the other authors.

Publication V: "Hydrophobic Nanocellulose Aerogels as Floating, Sustainable, Reusable, and Recyclable Oil Absorbents"

The author took part in designing the concept, designed and performed the experiments together with M.Sc. Marjo Kettunen, and analyzed the data. The author wrote the first draft of the manuscript and edited the revisions based on the input from the other authors.

List of Other Publications

The author has also contributed to the following related articles.

VI J. DE WIT, G. A. VAN EKENSTEIN, E. POLUSHKIN, J. KORHONEN, J. RUOKOLAINEN, and G. TEN BRINKE

Random Copolymer Effect in Self-Assembled Hydrogen-Bonded P(S-co-4VP)(PDP) Side-Chain Polymers.

Macromolecules, 42, 2009–2014, 2009.

VII J. T. KORHONEN, T. VERHO, P. RANNOU, and O. IKKALA

Self-Assembly and Hierarchies in Pyridine-Containing Homopolymers and Block Copolymers with Hydrogen-Bonded Cholesteric Side-Chains.

Macromolecules, 43, 1507–1514, 2010.

VIII N. D. LUONG, U. HIPPI, J. T. KORHONEN, A. J. SOININEN, J. RUOKOLAINEN, L.-S. JOHANSSON, J.-D. NAM, L-H. SINH, and J. SEPPÄLÄ

Enhanced Mechanical and Electrical Properties of Polyimide Film by Graphene Sheets via In Situ Polymerization.

Polymer, 52, 5237–5242, 2011.

IX N. D. LUONG, N. PAHIMANOLIS, U. HIPPI, J. T. KORHONEN, J. RUOKOLAINEN, L.-S. JOHANSSON, J.-D. NAM, and J. SEPPÄLÄ

Graphene/Cellulose Nanocomposite Paper with High Electrical and Mechanical Performances.

Journal of Materials Chemistry, 21, 13991–13998, 2011.

X T. HIRVIKORPI, M. VÄHÄ-NISSI, A. HARLIN, M. SALOMÄKI, S. AREVA, J. T. KORHONEN, and M. KARPPINEN

Enhanced Water Vapor Barrier Properties for Biopolymer Films by Polyelectrolyte Multilayer and Atomic Layer Deposited Al_2O_3 Double-Coating.

Applied Surface Science, 257, 9451–9454, 2011.

XI A. J. SOININEN, A. RAHIKKALA, J. T. KORHONEN, E. I. KAUPPINEN, R.

MEZZENGA, J. RAULA, and J. RUOKOLAINEN

Hierarchical Structures of Hydrogen-Bonded Liquid-Crystalline Side-Chain Diblock Copolymers in Nanoparticles.

Macromolecules, 45, 8743–8751, 2012.

XII M. WANG, I. V. ANOSHKIN, A. G. NASIBULIN, J. T. KORHONEN, J. SEITSONEN, J. PERE, E. I. KAUPPINEN, R. H. A. RAS, and O. IKKALA

Modifying Native Nanocellulose Aerogels with Carbon Nanotubes for Mechanoresponsive Conductivity and Pressure Sensing.

Advanced Materials, 25, 2428–2432, 2013.

XIII N. D. LUONG, J. T. KORHONEN, A. J. SOININEN, J. RUOKOLAINEN, L.-S. JOHANSSON, and J. SEPPÄLÄ

Processable Polyaniline Suspensions Through In Situ Polymerization onto Nanocellulose.

European Polymer Journal, 49, 335–344, 2013.

XIV H. VAHLMAN, J. HALME, J. KORHONEN, K, AITOLA, and J. PATAKANGAS

On the Mass Transport in Apparently Iodine-Free Ionic Liquid Polyaniline-Coated Carbon Black Composite Electrolytes in Dye-Sensitized Solar Cells.

The Journal of Physical Chemistry C, 117, 11920–11929, 2013.

Abbreviations and Symbols

α	Sliding angle, °
α_{L}	Polarizability of liquid
α_{S}	Polarizability of solid
$\Delta\cos\theta$	Contact angle hysteresis
$\Delta\theta$	Contact angle hysteresis, °
$\Delta\theta_{\%}$	Contact angle hysteresis percentage, %
ΔA	Change in area
$\Delta G_{1\rightarrow 2}$	Change in surface free energy in a transition from state 1 to 2
Δp	Pressure difference, Pa
Δp_{c}	Critical pressure, Pa
$\Delta p_{\mathrm{Y–L}}$	Laplace pressure, Pa
δU	Variation in internal energy
γ, σ	Surface tension, mJ/m^2 or mN/m
γ_{SL}	Solid–liquid interfacial tension, mJ/m^2
γ_{SV}	Solid–vapor interfacial tension, surface free energy, mJ/m^2
λ_{c}, κ^{-1}	Capillary length, mm
μ	Chemical potential
Ω	Grand potential
ρ	Density, mg/µl
τ	Adhesion tension, mJ/m^2
θ, CA	Contact angle, Young's contact angle, °
$\theta^{\star}$	Apparent contact angle, °
θ_{A}, ACA	Advancing contact angle, °
$\theta^{\star}_{\mathrm{CB}}$	Apparent contact angle of the Cassie–Baxter state, °
θ_{ms}, MSCA	Most-stable contact angle, °
θ_{R}, RCA	Receding contact angle, °
$\theta^{\star}_{\mathrm{W}}$	Apparent contact angle of the Wenzel state, °
A	Area

A_{geom}	Geometric area, *i.e.* horizontal projection of area
C	Curvature, typically mm^{-1}
$C \rightarrow W$	Cassie–Baxter to Wenzel wetting transition
F	Force, shear force, N
F_γ	Force exerted by surface tension force, N
f_1	Fraction of solid contact in the Cassie–Baxter equation
f_2	Fraction of water on air cushion in the Cassie–Baxter equation
F_{CAH}	Contact angle hysteresis force, N
F_{g}	Gravitational force along plane, N
F_{p}	Force exerted on water–air interface by external pressure, N
G	Free energy
g	Gravitational acceleration, 9.81 m/s^2
$G_{\text{C}\rightarrow\text{W}}$	Surface free energy change going from the Cassie–Baxter to the Wenzel state
G_{CB}	Surface free energy in the Cassie–Baxter state
G_{W}	Surface free energy in the Wenzel state
h	Height of a post
L	Length of a contact line, mm
n	Number of entities, such as atoms
p	Pitch, *i.e.* structure–to–structure distance
p	Pressure, Pa
p_0	Reference pressure, typically atmospheric pressure 101.3 kPa
R	Radius or radius of curvature, typically mm
r	Roughness factor in the Wenzel equation
r_{p}	Width of (the base of) a post in a wetting system
S	Spreading parameter
s	Path length, mm
V	Volume, typically µl
V_{crit}	Critical volume for sliding, µl
W_{A}	Work of adhesion
x	$\cos\theta$

1. Introduction

"Blow a soap bubble, and observe it. You may study it all your life, and draw one lesson after another in physics from it."
– Lord Kelvin

This thesis builds around the concept of *wetting phenomena*. Whether you realize it or not, wetting systems surround all of us (see Figure 1.1). For example, spilled coffee stains a piece of paper on my desk. A dark ring that is characteristic for such a stain occurs due to capillary flow along the drop surface together with pinning caused by *contact angle hysteresis*.[1–3] The latter phenomenon turns out as an important factor later on in this study. As a child, I remember watching as rain drops attached to the side windows of a bus — again due to contact angle hysteresis — and then suddenly starting to flow downwards, gaining speed as they grew larger due to coalescence with other drops.[4] Soap bubbles are an excellent manifestation of the effects of *surface tension* and *Laplace pressure*.[5] They are soap–water films that could be as thin as tens of nanometers and they exhibit interesting behavior, such as that when two bubbles collide, the smaller one might empty itself into the larger one.[6–8] Opening a faucet by a small amount results in a stream of water, which rapidly breaks into separate drops — a phenomenon known as Plateau–Rayleigh instability.[9–11] In fact, even the basis of milk homogenization lies within this instability,[8] since it facilitates breaking liquids into discrete particles of quantized size. "Tears of wine"[12] presents another interesting phenomenon caused by a wetting instability,[13,14] which occurs due to a surface tension gradient developing because of evaporation of ethanol from the wine. Many of us nowadays have water-proof clothing, whose water-repellency is based on a fluorinated semi-permeating film, such as Gore-Tex®.[15] On these pieces of clothing, water drops remain almost spherical and thus roll-off extremely easily, while allowing the fabric to "breathe" through its micro-pores. Another interesting wetting phenomena seen most often in the kitchen, is called the *Leidenfrost* effect.[16,17] On a hot iron plate, such as found on stoves, a drop of water remains spherical and bounces around the hot surface for a surprisingly long time. The drop does not boil because an insulating layer of gas forms beneath the drop and reduces the heat transfer. Furthermore, the gas escaping from below the drop causes it to

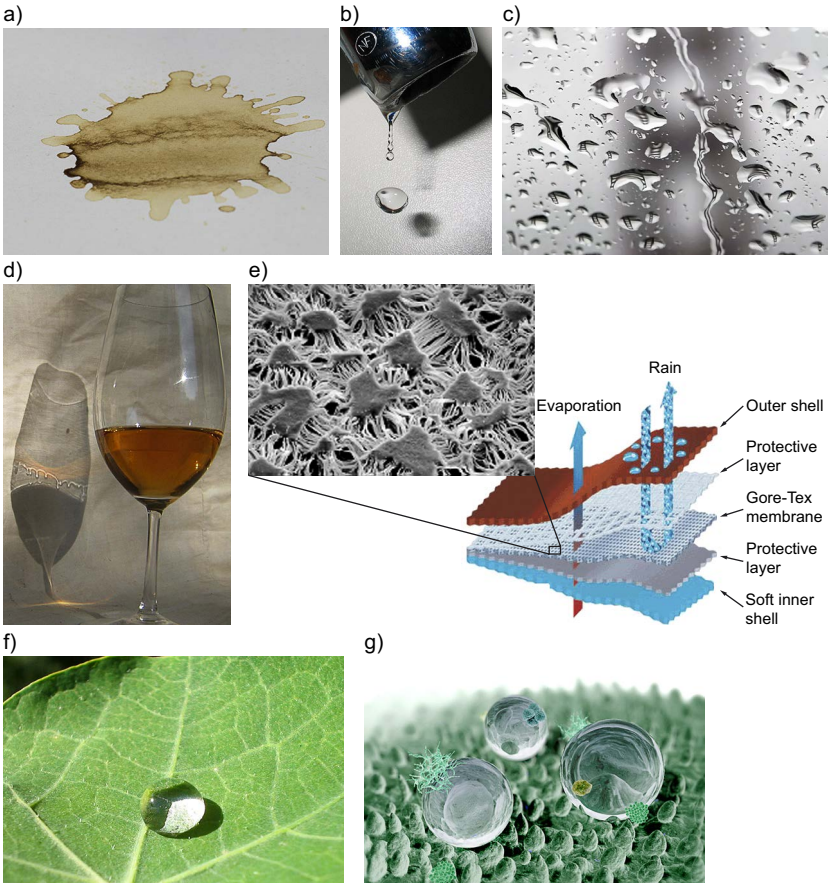

Figure 1.1. Various wetting phenomena demonstrated. a) A coffee stain with characteristic dark edges. b) Water dripping from a faucet. c) Water drops on a window. d) "Tears of wine" projected on a canvas. e) Scanning electron micrograph of a Gore-Tex® membrane along with a schematic representation. f) Water drop lying on a lotus leaf. g) Self-cleaning effect, where a water drop catches particles from a surface. Images used with permission from various sources. [18]

chaotically move around the plate. These are only a few of the endless examples of wetting phenomena found in our everyday lives and, being a physicist, I find myself especially intrigued by the possibilities offered.

In the 1990s, German botanical scientists, Wilhelm Barthlott and Christoph Neinhuis studied various plant leaves by the means of scanning electron microscopy. They noticed that smooth leaves had to be always cleaned prior to examination while those with epicuticular wax crystals on the surface did not. The resulting article with an almost poetic title, "*Purity of the Sacred Lotus, or Escape from Contamination on Biological Surfaces*", [19] (see Figure 1.1) quickly became the most cited reference relating *superhydrophobicity** to surface structure. Although the relation between surface roughness and water repellency

**Superhydrophobicity* refers to the extreme water repellency and self-cleaning ability of a surface. It is discussed in detail in Section 2.5.

has been known for long,[20,21] they were the first ones to explicitly quantify it experimentally and also to provide verification for the self-cleaning process. Since then the leaf microstructure of a lotus plant has been extensively mimicked to create artificial superhydrophobic surfaces.[22]

Since research on superhydrophobicity has grown, the accurate quantification of surface wetting properties has become extremely important. One of the challenges yet to fully overcome, is the method of measuring the thermodynamic contact angle of a surface, which is required to relate theoretical analyses to experimental data. Meanwhile, experimentalists are obliged to measure a range of applicable contact angles, which sometimes proves difficult. Furthermore, the nomenclature and even some fundamental concepts, such as the Cassie–Baxter equation or capillary rise, among the field are not yet fully established and especially the word "superhydrophobic" has been extensively misused.[23–32] Therefore, even today, there remains a need for studies on the principal phenomena around wetting and contact angles.

1.1 Outline of the Thesis

This thesis demonstrates how fundamental concepts from wetting and superhydrophobicity can be applied to different systems to create and analyze materials and surfaces with interesting properties. An emphasis is put on both theoretical understanding of the underlying physics as well as phenomenological studies of new materials. Furthermore, experimental materials can be divided into two groups. First comprises materials, which employ *silicone nanofilaments* as the hydrophobicing agent, and the second consists of *nanocellulose aerogels*, coated by *atomic layer deposition* with an inorganic shell. A schematic representation of these approaches is given in Figure 1.2.

Chapter 2, *Theory*, presents fundamental concepts about liquids on surfaces, starting from Young's law, through the works of Wenzel, and Cassie and Baxter, and finally arriving at the self-cleaning nature of a lotus leaf. The chapter continues with the concept of contact angles and especially advancing and receding contact angles, and presents a theory behind measuring the latter one, as described in Publication I. Later, a theory encompassed in Publication III describes the physics of contact lines and energetics of wetting phase transitions in the case of hierarchically wetting surfaces.

Chapter 3, *Experimental Results*, contains more than simply a list of used experimental methods. Instead, the chapter presents the experimental setup along with a detailed phenomenological model for the synthesis of silicone nano-

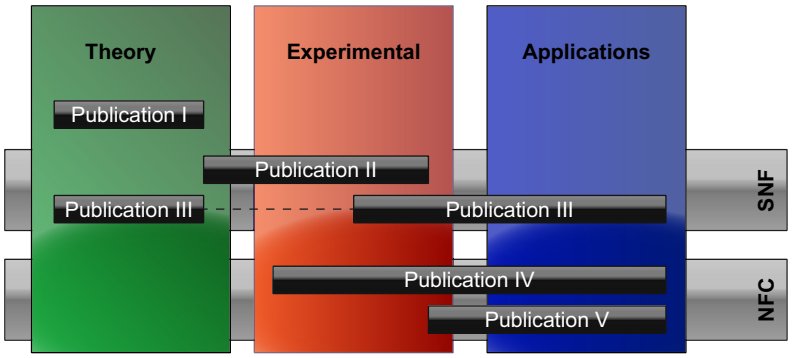

Figure 1.2. Schematic representation of the ways in which the publications are arranged throughout this thesis. The horizontal axis corresponds with the chapter arrangement and the vertical axis displays the two main experimental components, namely silicone nanofilaments (SNF) and nanofibrillated cellulose (NFC).

filaments, as described in Publication II. Data from Publications IV and V depict different preparation methods for nanocellulose aerogels as well as the procedure in which an inorganic shell was created using atomic layer deposition.

An important part of the thesis is described in Chapter 4, *Applications*, which demonstrates in which ways the materials with controlled wetting properties can be used to create functionalities. From a fundamental point of view, it was possible to create a surface, which can store and display information on its surface using nothing but water and trapped air, as portrayed in Publication III. In addition, the chapter describes functionalized nanocellulose aerogels, which display interesting wetting-based phenomena. Publication IV characterizes a titanium dioxide -nanotube film exhibiting a fast electric response to atmospheric humidity, and Publication V presents a selective oil-absorbent sponge, which could be used to harvest oil from the surface of water.

Finally, Chapter 5, *Conclusions*, provides a summary of the aspects, which were learnt during the study, and issues insights into concepts, which might be of interest when planning future research.

This study was done in collaboration between several researchers and research groups and credit for the ideas and work is given where the credit is due.

2. Theory

"An ounce of practice is worth a ton of theory."
– An English proverb

Water and water drops display a variety of marvels, ranging from the shape of rain drops, to soap bubbles and to the instability of thin liquid jets. To understand these interesting phenomena, a research field called capillarity (or wetting) emerged. In the early 1800s, Pierre Simon de Laplace and Thomas Young formed the basis of the field by developing some of the basic concepts, which have the most striking repercussions. When two immiscible fluids are in contact with each other, they act to minimize their surface free energy by deforming the contact area and their own shape. The bulk of the fluids exhibits cohesion energy, which stems from the van der Waals- and other interactions (such as hydrogen bonding) between the constituent molecules. Figure 2.1a displays a molecule at the interface between two fluids that "feels" only roughly half of the interaction energy and finds that the attractive self-interactions are replaced by repulsive interactions. This *interfacial tension* (or equivalently *interfacial free energy*) is a direct consequence of this lack of cohesion energy at the interface. When the surrounding fluid is air and the second fluid is liquid, the interfacial tension is instead called *surface tension* (or *surface free energy*) and it is denoted by the symbol γ (sometimes also σ). It expresses how much energy is needed to increase the liquid surface area by one unit, which leads to the thermodynamic definition $\gamma = \left[\frac{\partial G}{\partial A}\right]_{T,V,n}$.[8] Its value is proportional to the cohesion energy of the liquid and it is measured equivalently either in mJ/m^2 or mN/m. Typical van der Waals liquids, such as oils, exhibit a surface tension of $\gamma \approx 20$ mN/m, which is on the order of $k_\mathrm{B}T$. Ethanol, which is a polar solvent, comprises $\gamma \approx 23$ mN/m, and water, which is strongly hydrogen-bonded liquid exhibits a surface tension of $\gamma \approx 72$ mN/m.[8] The high surface tension of water is responsible for many of the interesting phenomena in drops and other liquid surfaces.

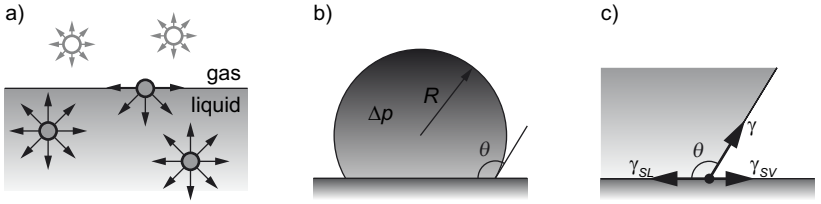

Figure 2.1. Surface tension, Laplace pressure, and Young's equation for contact angle demonstrated. a) A liquid molecule at the surface "feels" roughly half of the attractive interactions compared to molecules in the bulk. b) A small drop of water on a surface assumes a spherical cap shape with an angle of contact, θ, radius of curvature, R, and Laplace pressure, Δp. c) Three tensions (forces) are acting on the line of contact, solid–liquid interfacial tension acts towards the liquid, solid–vapor interfacial tension acts in the opposite direction, and liquid surface tension is directed along the drop surface. The Young's equation is formed when the horizontal components of these tensions are balanced.

2.1 Drops and Spreading

Since creating a surface on a liquid costs energy, in the absence of external forces, a drop suspended in a medium (such as air or oil) adopts its minimal surface, which is a sphere. However, the pressure inside the sphere has to be larger than outside to accommodate for the surface tension. The pressure difference is given by the *Young–Laplace* equation,

$$\Delta p = \gamma C = \gamma \left(\frac{1}{R_1} + \frac{1}{R_2} \right), \tag{2.1}$$

where C is the curvature of the surface, and R_1 and R_2 are the principal radii of curvature (see Figure 2.1b). Equation (2.1) can be derived for a simple system of a spherical water drop in air, by considering a grand potential of the form $\Omega = F - \sum_{\mathrm{i}} n_{\mathrm{i}} \mu_{\mathrm{i}} = -p_0 V_0 - p_{\mathrm{w}} V_{\mathrm{w}} + \gamma A$.[8] Minimizing Ω by $\frac{d\Omega}{dR} = 0$ yields $\Delta p = p_{\mathrm{w}} - p_0 = \frac{2\gamma}{R}$, which is the Young–Laplace equation. When curvature, C, is constant throughout the surface (as in the case of a sphere), the Laplace pressure is also constant, and vice versa. Furthermore, small drops have a higher Laplace pressure than larger ones, which indicates that, when connected, liquid from the small drops flows into the larger one. This effect has dramatic implications, such as Ostwald ripening of micro-emulsions, like the ones seen when certain alcoholic beverages are mixed with water (*i.e.* the *ouzo effect*); and the stability of lung alveoli during respiration, which is facilitated by the presence of a surfactant. The Young–Laplace equation is also one of the most important tools when calculating phase- and contact line transitions in wetting systems.

An important question about a surface is whether water is going to wet it. This can be assessed by the spreading parameter, S, which indicates the surface

free energy difference of a wetted surface compared to a dry surface:

$$S = \gamma_{SV} - \left(\gamma + \gamma_{SL}\right), \tag{2.2}$$

where γ_{SV}, γ_{SL}, and γ are the solid–vapor and solid–liquid interfacial tensions, and the surface free tension (of water). If the surface free energy of a dry solid is larger than the wetted one, *i.e.* $S > 0$, water wets the surface and the situation is depicted as *total wetting*. In this case the contact angle (which is discussed below) will be exactly zero. Every other case falls into *partial wetting* regime, where $S < 0$. In this situation water adopts a non-zero contact angle and drops can form on the surface. Partially wetting surfaces can be further divided into hydrophilic, hydrophobic, and superhydrophobic subclasses, yet the limits for these cannot be determined from the spreading parameter. Instead, the concept of a contact angle needs to be employed.

2.2 Theorems of Young, Wenzel, and Cassie–Baxter

In 1805 Thomas Young presented that when a liquid is in contact with a surface, it adopts an angle of contact, which is dependent on the interfacial tensions of the constituent three phases, namely solid, liquid, and air (vapor).[33] Albeit Young did not employ equations, this notion can be written in the form, which is denoted as Young's equation:

$$\gamma \cos\theta = \gamma_{SV} - \gamma_{SL}, \tag{2.3}$$

where γ_{SV} and γ_{SL} represent the solid–vapor and solid–liquid interfacial tensions, respectively, and γ equals the surface tension of the liquid. Perhaps the most intuitive method to derive Young's equation is to consider the three interfacial tensions (forces) occurring at the triple-phase boundary line (see Figure 2.1c). At equilibrium, the sum of the horizontal components of these tensions has to equal zero, *i.e.* $\gamma\cos\theta + \gamma_{SL} - \gamma_{SV} = 0$, which immediately yields Young's equation. Later, Johnson used surface thermodynamics to derive the equation rigorously.[34] The final result yielded six different equations, including Young's equation, which all have to be satisfied. Another popular, yet criticized,[35] derivation is to consider the change in internal energy of the system when contact line advances slightly, $\delta U = \gamma_{LV}\delta A_{LV} + \left(\gamma_{SL} - \gamma_{SV}\right)\delta A_{SL}$. Geometrical considerations lead to $\delta A_{LV} = \delta A_{SL}\cos\theta$, and applying $\delta U = 0$ for small perturbations, yields $\left[\gamma_{LV}\cos\theta + \left(\gamma_{SL} - \gamma_{SV}\right)\right]\delta A_{SL} = 0$, which produces Young's

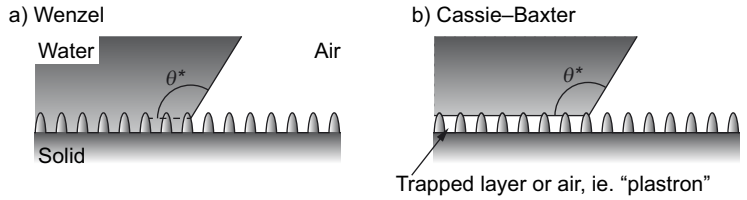

Figure 2.2. Wetting states of a rough surface. a) Water protrudes the roughness features in the Wenzel state. b) An air cushion remains trapped below the water in the Cassie–Baxter wetting state.

equation. Furthermore, the equation has been derived also from local surface thermodynamics.[35] In conclusion, Young's equation is a well established law, yet the most common form only applies when the surface is chemically homogeneous, inert, hard, and smooth. To accommodate for surface roughness, additional aspects have to be taken into account.

In 1936 Wenzel published a seminal study on how surface roughness influences the apparent (observed) contact angle.[36] The different contact angles are discussed in detail later, yet at this point it is adequate to notice that the apparent contact angle differs from the local Young's contact angle (defined by Equation (2.3)), which follows the microscopic roughness of the surface (see Figure 2.2a). A roughness factor is defined as $r = A/A_{\mathrm{geom}}$, where A is the actual surface area and A_{geom} is the perpendicular projection of A. It should be noted that this roughness factor does not correspond with the *rms* roughness of a solid.[37] Adhesion tension, which is defined as

$$\tau = \gamma \cos\theta, \tag{2.4}$$

basically indicates the tension needed to oppose the horizontal component of the surface tension. Wenzel considered an equivalent surface where τ is multiplied by the roughness, r, which yields $r\tau = r\left(\gamma_{\mathrm{SV}} - \gamma_{\mathrm{SL}}\right) = \gamma\cos\theta^{\star}$, where $\theta^{\star}$ is the apparent contact angle. Replacing Young's equation produces Wenzel's equation,

$$\cos\theta^{\star} = r\cos\theta, \tag{2.5}$$

which relates Young's contact angle, θ, to the apparent contact angle, $\theta^{\star}$. Young's contact angle of a smooth surface has been shown to reach up to *ca.* 120°,[38] which implies that a roughness factor of $r = 2$ is adequate to render the apparent contact angle 180°. Similarly, an apparent contact angle of 0° is achieved for rough hydrophilic surfaces. It is evident that with extremely rough, hydrophobic surfaces, the apparent (Wenzel) contact angle can exceed 180°. Obviously this is not physically possible, yet composite wetting occurs, which implies that

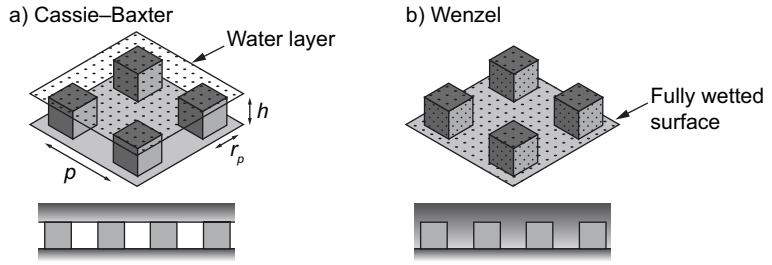

Figure 2.3. Square lattice of cubical posts. a) In the Cassie–Baxter state water touches only the tops of the posts. b) The entire surface is wetted in the Wenzel state.

a part of the surface under the drop remains dry.

The composite wetting regime was addressed in 1944 by Cassie and Baxter,[39] who considered a system where fraction f_1 of water wets the surface, yet fraction f_2 lies on top of an "air cushion" (see Figure 2.2b). The net energy of creating a wetting surface per unit area can be expressed as $G = f_1\left(\gamma_{SL} - \gamma_{SV}\right) + f_2\gamma$. With the help of Young's equation (2.3) this can be written as $G = \gamma(f_2 - f_1\cos\theta)$, and the apparent contact angle can be defined as $\cos\theta^\star = \left(\gamma_{SV} - \gamma_{SL}\right)/\gamma = -G/\gamma$, which combined with previous results in the *Cassie–Baxter* equation,

$$\cos\theta^\star = f_1\cos\theta - f_2. \tag{2.6}$$

It can be seen that increasing the air fraction, f_2, yields higher apparent contact angles regardless of the Young's contact angle. This effect has been employed in creating surfaces exhibiting composite wetting for materials which exhibit intrinsic contact angles less than 90°.[40] However, not all values of f_2 are stable, which becomes apparent when $f_2 \to 1$ as the drop should lie on top of nothing but air. In addition, when $f_2 = 0$, the Cassie–Baxter equation (2.6) reduces to the Wenzel equation (2.5) with $f_1 = r$, and for strictly horizontal interfaces $f_2 = 1 - f_1$. In general, the more stable wetting state (either Wenzel or Cassie–Baxter) is determined by which exhibits the lower apparent contact angle.[41] However, the Cassie–Baxter state may be kinetically trapped into a metastable state, even when the Wenzel state would be energetically favorable.[42] Furthermore, in certain systems, transitions between the two wetting regimes can occur either spontaneously or they may be induced by an external stimulus.[42–47]

2.3 Wetting Transitions

The most simple way to evaluate wetting transitions is to calculate the surface free energy changes between two distinct states. The energy required to wet a surface can be evaluated by multiplying the interfacial free energy by the wetted area. The Wenzel and Cassie–Baxter states in Figure 2.3 act as model system, and let us consider a simple transition from the Cassie–Baxter state to the Wenzel state, hereafter denoted as $C \rightarrow W$. The shape of the posts is a cube with sides of width, r_{p}, height, h, and post–to–post distance (pitch) of p. In the Cassie–Baxter state water touches the tops of the pillars and lies on an air cushion elsewhere. The surface free energy can be written as:

$$G_{\mathrm{CB}} = \gamma_{\mathrm{SL}} A_{\mathrm{SL}}^{\mathrm{CB}} + \gamma A_{\mathrm{LV}}^{\mathrm{CB}} + \gamma_{\mathrm{SV}} A_{\mathrm{SV}}^{\mathrm{CB}}. \tag{2.7}$$

Similarly, in the Wenzel state, the whole surface is wetted, and surface free energy becomes:

$$G_{\mathrm{W}} = \gamma_{\mathrm{SL}} A_{\mathrm{SL}}^{\mathrm{W}}. \tag{2.8}$$

The transition energy from the Cassie–Baxter to the Wenzel state can be written as:

$$G_{\mathrm{C}\rightarrow\mathrm{W}} = G_{\mathrm{W}} - G_{\mathrm{CB}} = \gamma_{\mathrm{SL}} \left(A_{\mathrm{SL}}^{\mathrm{W}} - A_{\mathrm{SL}}^{\mathrm{CB}} \right) - \gamma A_{\mathrm{LV}}^{\mathrm{CB}} - \gamma_{SV} A_{\mathrm{SV}}^{\mathrm{CB}}, \tag{2.9}$$

which using Equation (2.3) and noting that $A_{\mathrm{SL}}^{\mathrm{W}} - A_{\mathrm{SL}}^{\mathrm{CB}} = A_{\mathrm{SV}}^{\mathrm{CB}}$ reduces to

$$G_{\mathrm{C}\rightarrow\mathrm{W}} = -\gamma \left(A_{\mathrm{LV}}^{\mathrm{CB}} + A_{\mathrm{SV}}^{\mathrm{CB}} \cos\theta \right). \tag{2.10}$$

For simplicity, let $h = r_{\mathrm{p}}$ and $p = 2r_{\mathrm{p}}$, which results in

$$G_{\mathrm{C}\rightarrow\mathrm{W}} = -\gamma \left(7r_{\mathrm{p}}^2 \cos\theta + 3r_{\mathrm{p}}^2 \right). \tag{2.11}$$

The Cassie–Baxter state is energetically favorable when the transition energy is positive, $G_{\mathrm{C}\rightarrow\mathrm{W}} > 0$, which yields a geometric inequality $\theta \gtrsim 115°$. Interestingly, the result depends neither on the actual value of r_{p} nor the used fluid (no γ–dependence). If the intrinsic Young's contact angle is known, Equations (2.5) and (2.6) can evaluate the apparent contact angles, using $f_1 = \frac{1}{4}$, $f_2 = \frac{3}{4}$, and $r = 2$. For a reasonably hydrophobic surface, whose $\theta = 110°$, the apparent contact angles yield $\theta_{CB}^{\star} \approx 147°$ and $\theta_{W}^{\star} = 133°$. However, this reasoning yields no information about whether a phase transition should occur. For that end, the stability of the Cassie–Baxter state needs to be evaluated through a force-balance mechanism.

A transition from CB to W can occur by two routes. The first route is through destabilization of the meniscus and the second is through an external force. Consider a post system with vertical walls, such as in Figure 2.4a. When the water–air interface moves downwards the contact angle adopts on the vertical surface. For $\theta < 90°$ the interface has to curve upwards (in this system), which indicates a *negative* Laplace pressure. Since pressure inside the meniscus is higher than outside, the depicted situation is terminally unstable and the system collapses to the fully wetting Wenzel state. The second process involves an external force, which in the simplest case is pressure (see Figure 2.4b). Internal Laplace pressure, $\Delta p_{\text{Y–L}}$, curves the water–air interface downwards and the contact angle at the edge of the post has to adopt correspondingly to the equilibrium contact angle, θ. The pressure exerts a force of

$$F_{\text{Y–L}} = A_{\text{LV}} \Delta p_{\text{Y–L}} \tag{2.12}$$

on the meniscus, which is countered by surface tension force at the post edges

$$F_\gamma = L\gamma \cos\theta_{\text{eq}}, \tag{2.13}$$

where L is the length of the contact line around the post, and θ_{eq} is the equilibrium contact angle. Additionally, an external pressure, Δp, pushes on the meniscus by force:

$$F_{\text{p}} = A_{\text{LV}} \Delta p. \tag{2.14}$$

Right before the contact line starts to move, it is countered by a force, which is related to the highest non-equilibrium contact angle the surface can uphold, *i.e.* the *advancing* contact angle (the different contact angles are discussed in detail later).

$$F_\gamma = \gamma \left(\cos\theta_{\text{eq}} - \cos\theta_{\text{A}}\right) L. \tag{2.15}$$

This force is equal to $F_\gamma = F_{\text{p}} + F_{\text{Y–L}}$. Subtracting the internal Laplace pressure from the required pressure to move the contact line yields a critical external pressure condition for the second process:

$$F_{\text{p}} = F_\gamma - F_{\text{Y–L}} \tag{2.16}$$

$$\Rightarrow \Delta p_{\text{c}} = -L\gamma \cos\theta_{\text{A}} / A. \tag{2.17}$$

Replacing the geometric values for the square lattice of cubes, $r_{\text{p}} = 10$ µm, surface tension of water ($\gamma \approx 71.97$ mN/m), and $\theta_{\text{A}} = 125°$ yields $\Delta p_{\text{c}} = 5.5$ kPa, which corresponds to the hydrostatic pressure of a *ca.* 55 cm high water col-

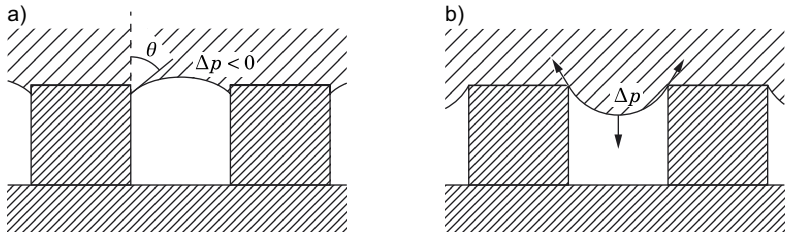

Figure 2.4. Force balance on a post system (geometry exaggerated). a) For excessively low contact angles, the pressure inside the meniscus becomes negative, which renders the system unstable. b) Laplace pressure Δp induces a downward force on the water–air interface and interfacial tension force at the post edge opposes it. The force arrows indicate the forces exerted on the water–air interface.

umn. The result indicates that the original state remains more stable until an overpressure of 5.5 kPa is reached.

2.4 Contact Angles and Hysteresis

As was already mentioned, a variety of contact angles exists.[26] The ones relevant to this work are briefly discussed below. The *Young's* contact angle (CA, θ) was already mentioned and it is the one defined by Young's equation (2.3). Here it is also called the *intrinsic* contact angle, which defines the contact angle of the surface excluding the effects of roughness or chemical heterogeneity. *Geometric* contact angle (or simply "contact angle", also θ) is used in calculations to represent any possible (or even impossible) Young's contact angle. *Apparent* contact angle ($\theta^\star$) is the one, which is macroscopically measured on a rough surface and it usually can be evaluated through the Wenzel (2.5) or Cassie–Baxter equations (2.6). *Most stable* contact angle (MSCA, θ_{ms}) is defined as the contact angle, which is thermodynamically most stable. This is the value that should be reported, yet it has turned out to be challenging to measure.[48–51] Instead, so-called *advancing* (ACA, θ_{A}) and *receding* (RCA, θ_{R}) contact angles are typically reported. Due to contact line pinning and surface heterogeneity there exists a range of metastable contact angles, which can be measured experimentally (the process of measuring the RCA is discussed in detail later). In addition, there are also *dynamic* contact angles, which occur when the liquid contact line is moving at a significant velocity. The aspect of moving non-curving contact lines has been dealt with theoretically, experimentally, and by means of simulations, yet no simple form for moving contact lines of drops has been demonstrated.[52–58]

In order to explain advancing and receding contact angles, it is necessary to describe the basics of contact angle measurements (a more thorough method

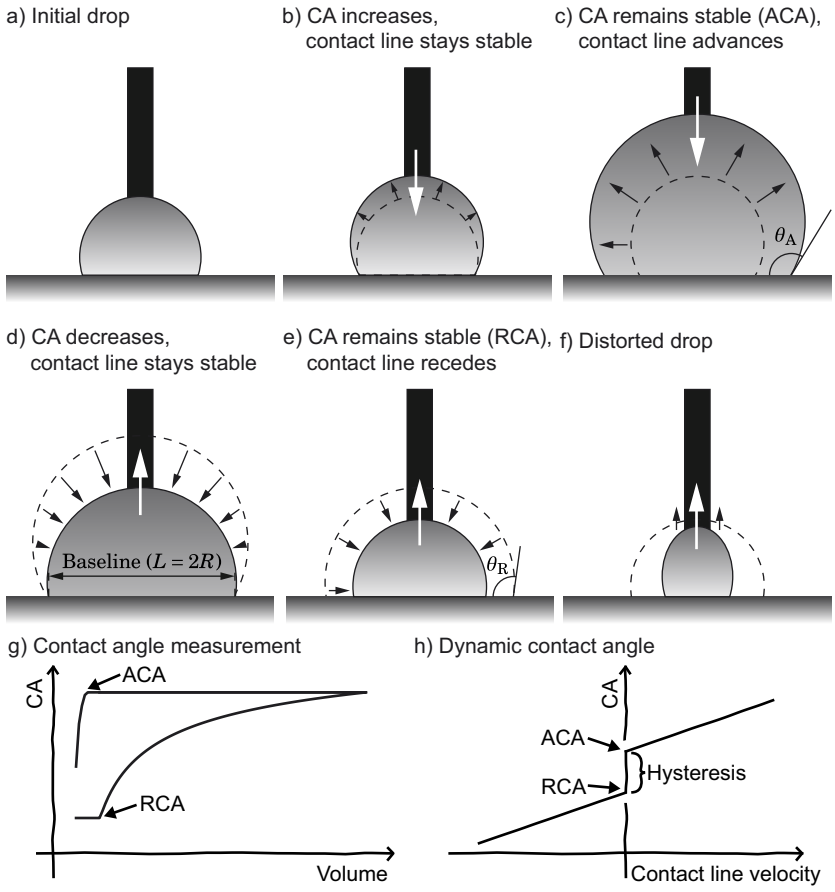

Figure 2.5. Basic procedure for measuring the advancing (ACA) and receding contact angles (RCA). a) An initial, as-deposited drop with a needle. b)-c) Volume of the drop is increased until the advancing contact angle is reached. d)-e) Volume is decreased until the RCA is reached. f) Distortions often occur for small drops. g) Example of a contact angle measurement, where volume is first increased and ACA is reached, followed by volume decrease and RCA. h) Contact angle as a function of contact line velocity. The ACA and RCA occur at zero velocity and they are thus static contact angles. Adapted with permission in part from Publication I.

is given in Chapter 3). Figure 2.5 shows schematically the way in which a *sessile drop* contact angle measurement proceeds. Briefly, a drop of water is deposited on the studied surface, where it adopts an unspecified contact angle (Figure 2.5a). The contact angle is, in general, not the MSCA, since the method of drop deposition affects the result. To measure the MSCA, more complicated methods, such as mechanical vibration[48–50] or tilting-plates,[51] have to be employed. The ACA is reached by increasing the drop volume as long as the contact angle increases (Figure 2.5c) and taking the saturation value. Correspondingly, RCA is reached by decreasing the drop volume (Figure 2.5e). The ACA is thus the highest measurable (static) contact angle and RCA is the lowest (static) contact angle. They are trapped metastable states, as there exists a global minimum somewhere in between the two. However, these states may exhibit long lifetimes. Another way to define the angles is to consider an experiment, where contact angles are probed against the movement of the contact line (Figure 2.5h). At zero velocity, a range of contact angles coexist. This range defines the static contact angles and its limits are exactly the ACA and RCA. The region of metastable contact angles limited by ACA and RCA is called *contact angle hysteresis*.

Hysteresis refers to an effect where material properties depend on its history. In terms of wetting, contact angle hysteresis refers to the range of static contact angles a surface can uphold. It is most simply defined as $\Delta\theta = \theta_A - \theta_R$, yet this definition has little physical meaning. Sometimes $\Delta\cos\theta = \cos\theta_R - \cos\theta_A$ has been employed.[59] It is directly proportional to the force required to move a drop on a surface,[4] $F \sim \Delta\cos\theta$, yet its value ranges from 0 to 2, which makes it difficult to comprehend intuitively. Instead, Publication I proposes a "hysteresis percentage",

$$\Delta\theta_{\%} = \frac{\Delta\cos\theta}{2} \cdot 100\% = \frac{\cos\theta_R - \cos\theta_A}{2} \cdot 100\%, \tag{2.18}$$

which ranges from 0% (zero hysteresis) to 100% (full hysteresis). Full hysteresis represents a situation where $\theta_A = 180°$ and $\theta_R = 0°$, and zero hysteresis occurs for all combinations where $\theta_A = \theta_R$. The hysteresis percentage values for different contact angles can be directly compared to each other as the hysteresis percentage value does not depend on the actual contact angles. Further benefits emerge, for example, when considering the MSCA or wetting phase transitions.

A sessile drop on a surface will start to slide downwards when the surface is inclined at a certain angle, α, which depends on the properties of the surface and the drop. A simple derivation is given by considering the situation in Figure 2.6, where a drop resides on an inclined plane. Gravitational force pulls

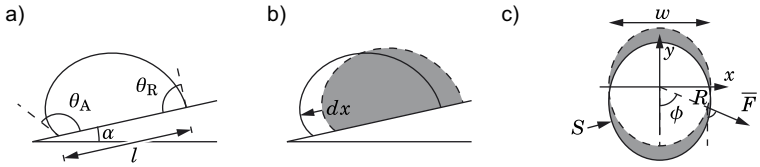

Figure 2.6. Geometry used in deriving the sliding angle. a) A plane is inclined by angle, α, and the contact angles at the extremes are θ_A and θ_R. b) The drop moves forward by distance dx. c) Drop from above. ϕ is the spherical coordinate, S is the length of the contact line, w is the drop width, R is the drop radius at ϕ, and $\vec{F}$ is the contact line force due to surface tension.

the drop downwards, which creates a sliding force $F_g = mg\sin\alpha$. Right before starting to slide, this force is opposed by a "contact angle hysteresis force", F_{CAH}. This force can be estimated by considering the projection of the force along the sliding axis. Without losing generality, the equation can be written in spherical coordinates,

$$\oint d\vec{f}\cdot\hat{e}_y = -\int_0^{2\pi}\left[\gamma\cos\theta - \left(\gamma_{SV}-\gamma_{SL}\right)\right]R\cos\phi d\phi. \tag{2.19}$$

Equation (2.19) can be simplified, when certain parameters, such as the shape of the contact line or the contact angle distribution, are known. For symmetric contact lines, the equation simplifies to $F_{CAH} = -\gamma\int_0^{2\pi} R\cos\theta\cos\phi d\phi$. By assuming that at the advancing front $\theta = \theta_A$ and at the receding front $\theta = \theta_R$, the integral can be split into two hemispheres. Further assuming a circular contact line, *i.e.* $R \neq R(\phi)$, the total force reduces to $F_{CAH} = 2\gamma R(\cos\theta_R - \cos\theta_A)$. Finally, the equilibrium right before sliding can be written

$$\sin\alpha = \frac{w}{V}\frac{\gamma}{\rho g}(\cos\theta_R - \cos\theta_A) = K\lambda_c^2 2\Delta\theta_{\%}, \tag{2.20}$$

where ρ is the density of water, g is gravitational acceleration, $w = 2R$ is the width of the drop, K is a term containing all the geometric parameters of the system, such as the mass of the drop and the length of the contact line, λ_c is the capillary length (2.7 mm for water), and the hysteresis percentage, $\Delta\theta_{\%}$, which was conveniently substituted into the equation. The geometric term varies depending on the derivation, for example, Furmidge[4] $K = w/V$ (drop profile is a rectangle), Rosano[60] $K = l/V$ (circular contact line), and Macdougall & Ockrent[61] $K = A^{-1}$, where w is the drop width perpendicular to the sliding axis, V is drop volume, $l = w$ is the drop contact diameter, and A is drop contact area. All of these approaches neglect the fact that only at the very edges of the advancing and receding fronts the maximum/minimum contact angle values are reached and the contact angle changes continuously as a function of ϕ. However, in many situations, the drop adopts a nearly rectangular shape,[4] and the

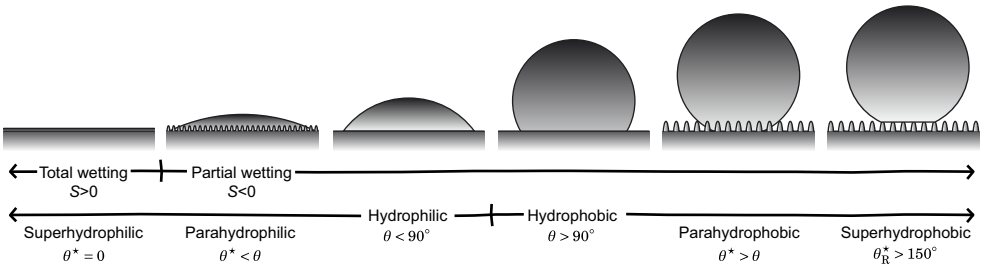

Figure 2.7. Schematic representation of wetting terminology. Spreading parameter, S, divides surfaces to total wetting and partial wetting. The sign of $\cos\theta$ defines hydrophilic (+) and hydrophobic (−) surfaces. Parahydrophilic and parahydrophobic indicate roughness-induced increase in the intrinsic property of the material. Superhydrophilic surfaces display exactly $\theta^\star = 0$ and $S > 0$. Superhydrophobic surfaces exhibit the Cassie–Baxter wetting state and $\theta_R > 150°$.

approximation becomes valid. Furthermore, the applicability of the equation needs to be estimated in each case separately.

2.5 Superhydrophobicity

In its simplest form, superhydrophobicity refers to extreme non-wettability of a surface by water. The origin of the term is unclear and there still exists no exact definition. Sometimes the term has been claimed[62] to have been first used by Onda *et al.* as late as 1996,[63,64] yet a little literature research shows that it has been used as an already established term as early as 1976.[65,66] To understand the special nature of superhydrophobicity, it is necessary to introduce a whole spectrum of wetting terminology. There exists numerous competing definitions and terminologies, whose popularity depends on aspects such as the author's field and background. The nomenclature used in this study mainly follows the terminology proposed by Marmur[32] along with a definition for superhydrophobicity, which was introduced in Publication I. Figure 2.7 demonstrates the employed definitions.

2.5.1 Hydrophobicity, Hydrophilicity

Young's equation (2.3) yields an intuitive, yet arbitrary, definition for hydrophilic and hydrophobic surfaces. As the cosine changes its sign exactly at $\theta = 90°$, it results in $\gamma_{SV} > \gamma_{SL}$ for hydrophilic and $\gamma_{SV} < \gamma_{SL}$ for hydrophobic surfaces. These inequalities indicate that hydrophilic surfaces are rather wetted than dry, and vice versa. However, there are other possibilities. One

definition is based on the *work of adhesion* given by the Dupré equation:

$$W_{\mathrm{A}} = \gamma_{SV} + \gamma - \gamma_{\mathrm{SL}} = \gamma(1 + \cos\theta), \tag{2.21}$$

which indicates the amount of energy required to dry a wetted surface. Since, in the study,[67] hydrophilic molecules exhibited a free energy of solvation, $\Delta G_{\mathrm{SL}} = -W_{\mathrm{A}}$, of < -113 mJm^{-2} in water, the limiting contact angle was defined as $\theta \approx 56°$.[62,67] Another approach defined hydrophilic surfaces as having water adhesion tension, τ (Equation (2.4)), of less than 30 mN/m, which results in a limiting angle of 65°.[68] This approach has gained some recent support,[69] and it has been claimed that polymer surfaces with $\theta > 65°$ exhibit Wenzel-type *increase* in contact angle, when roughened with sandpaper, and even a modified Wenzel equation has been proposed.[70] However, these results remain controversial, as it is not entirely clear whether the effect could have been due to increased hysteresis, since advancing and receding contact angles were not reported. The most simple definition based on the sign of the cosine is used in this study, since none of the other propositions yield additional benefits, and especially their compatibility with roughness-induced hydrophobicity asks for further clarifications.

2.5.2 Parahydrophobicity, Parahydrophilicity

The Wenzel equation (2.5) describes how roughness of a surface affects its apparent wetting properties. Currently, there exists no generally approved nomenclature for roughness-induced hydrophobicity and hydrophilicity. An attempt on clarification was introduced by Marmur,[32] who defined roughness-induced hydrophobicity as *parahydrophobicity*, which indicates hydrophobicity *beyond* (*i.e.* "para") what can be achieved by smooth surfaces. This approach has not yet gained general popularity. However, in lieu of a better solution, the *para*-approach is adopted here. Smooth surfaces, for which contact angle would be higher than 120°, remain unknown. Thus, surfaces with $\theta > 120°$, which are *not superhydrophobic*, are called parahydrophobic. Similarly, *parahydrophilic* surfaces can be defined as ones exhibiting apparent contact angles less than their Young's contact angles. There is no lower limit for smooth hydrophilic surfaces. Therefore, there is no requirement for the contact angle to exhibit a value less than some limiting angle. There remains controversy about these definitions, which has led to parahydrophobic surfaces being widely named superhydrophobic and parahydrophilic surfaces being confused with *superhydrophilicity*. Note also that smooth surfaces are never parahydrophilic, yet

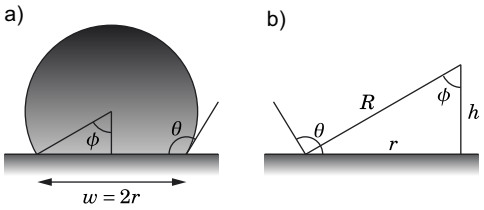

Figure 2.8. Geometry used in estimating the volume of spherical cap. a) A sessile drop on surface with contact angle, θ. b) Geometric relations of the different variables.

they can be superhydrophilic.

2.5.3 Traditional Definition of Superhydrophobicity

Superhydrophobic surfaces comprise a class of materials, which are characterized by extreme water repellency and a low roll-off angle for water. The most commonly employed definition for superhydrophobicity sets two requirements. The contact angle of the surface should be higher than 150° and the sliding angle of a drop on the surface should be less than 10°.[62–64,71] Sometimes the second requirement is phrased as "low sliding angle". As was stated earlier, superhydrophobicity is impossible to achieve through surface chemistry alone, yet surface roughness and Cassie–Baxter -type of wetting is required. The roughness can be on the microscopic level, nanoscopic level, or hierarchical.[19,63,64,72–74] Superhydrophobicity is observed in nature[19,72] as well as in man-made systems[63]. The traditional definition is incomplete in two ways. First, it does not state which contact angle should be measured. The most obvious choice would be the MSCA, yet it seems that in many cases the only reported value is a "static" contact angle, which bears no thermodynamic information. Second, the requirement for a low sliding angle is complicated by its dependence on numerous experimental parameters (see Equation (2.20)), such as the size of the drop and the type of surface roughness.[4,61,75]

2.5.4 Proposed Definition of Superhydrophobicity

Publication I proposes a novel definition for superhydrophobicity, namely that superhydrophobic surfaces *exhibit a receding contact angle higher than 150°*. While the choice of the limit in contact angle is arbitrary, this remarkably simple definition satisfies both the requirements of the traditional definition and states unambiguously which contact angle is the determining factor. The requirement for a low sliding angle can be assessed through Equation (2.20). Replacing values for water and assuming a spherical cap shape for the drop (*i.e.* gravity is neglected) yields an inequality $K\lambda_c 2\Delta\theta_{\%} < \sin\alpha_0$. Figure 2.8

depicts the geometry and parameters employed. The volume of a segment of a sphere can be written as $V = \frac{\pi}{3}h^2(3R-h)$, and the height of the segment $h = R\left(1-\cos\phi\right)$. Combining these with the volume of a sphere, $V_{\text{sphere}} = \frac{4}{3}\pi R^3$, and noting that $\phi = \theta - \pi/2$ leads to

$$V = V_{\text{sphere}} - V_{\text{segment}} = \frac{\pi}{3}R^3\left(x^3 - 3x + 2\right), \tag{2.22}$$

where $x = \cos\theta$, for simplicity. Using $w = 2r = 2R\sin\theta$, the width of the base of the drop may be written as:

$$w = V^{\frac{1}{3}}\left(\frac{24}{\pi}\right)^{\frac{1}{3}}\left(x^3 - 3x + 2\right)^{-\frac{1}{3}}\sqrt{1-x^2}, \tag{2.23}$$

which can be employed to estimate $K = \frac{w}{V} = V^{-\frac{2}{3}}f(\theta)$, where $f(\theta)$ is a function containing all the contact angle dependence. Inputting the values into the inequality, yields

$$V_{\text{crit}} = \left(\frac{f(\theta)\lambda_{\text{c}}^2(2\Delta\theta_{\%})}{\sin\alpha_0}\right)^{\frac{3}{2}} \tag{2.24}$$

Replacing pairs of contact angle values in the range from 150° to 180°, gives a maximum for the critical volume for sliding, which is *ca.* 5 µl for a sliding angle of 10°. Thus, the requirement that the receding contact angle is higher than 150° always leads to a sliding angle less than 10° for drops larger than 5 µl. For most contact angles the required volume is less than this value, since it is the "worst case" scenario. The proposed definition for superhydrophobicity is employed throughout this study and surfaces which exhibit inadequate hydrophobicity are simply termed parahydrophobic.

2.5.5 Superhydrophilicity

In addition to superhydrophobicity, another concept that has caused confusion is superhydrophilicity. On a smooth surface with a positive spreading parameter, S, water spreads completely and thus adopts a zero contact angle. This kind of surface is also called *superhydrophilic*. On a rough hydrophilic surface, the apparent contact angle is given by the Wenzel equation (2.5). Zero contact angle can be reached by satisfying $r\cos\theta > 1$. For $\theta = 60°$, roughness needs to equal 2 to reach zero apparent contact angle. The question remains, whether such a surface is superhydrophilic or merely parahydrophilic. An interpretation, that a surface with an apparent contact angle of exactly zero is superhydrophilic, is adopted here. However, in literature, surfaces and materials with "low" contact angles have been misleadingly denoted superhydrophilic. This has been

the case, especially with absorbing materials, such as sponges. The *dynamics* of the wetting process are different for surfaces where contact angle actually reaches zero than those with contact angle close to zero,[32,62] which calls for a distinction between the two cases. In this study, surfaces that do not satisfy the strict criterion are called parahydrophilic.

2.5.6 Oleophobicity, Oleophilicity

So far, this text has only considered water as the liquid phase. Also other liquids follow the same set of rules and equations, yet they are more prone to wetting the surfaces. There are two reasons behind this notion. Polar liquids of van der Waals -type wet a surface totally when the liquid is less polarizable than the surface,[8] which is governed by an approximate equation, $S = k(\alpha_S - \alpha_L)\alpha_L$, where the α_S and α_L denote the polarizabilities of the solid and liquid, respectively. However, for non-polar liquids, the spreading parameter is independent of the liquid, and only a function of the surface free energy, γ_{SV}. Here, an additional prefix of *oleo-* is employed to describe surface wetting by oils and non-polar solvents.* Oleophobicity refers to materials that repel *oils*. Because of the combination of high surface tension and high polarizability of water, surfaces are always more "phobic" towards water than oils.† Therefore, oleophobic materials are also hydrophobic. However, it is easy to find out that hydrophobic materials may well be oleo*philic*, which creates an interesting combination of water repellency and oleophilicity, which was utilized in Publication V.

2.6 Theory of Contact Angle Measurements

Contact angle on a surface is a manifestation of the Young's equation, $\gamma\cos\theta = \gamma_{SV} - \gamma_{SL}$. There are four independent variables, one of which can be readily measured (in a single measurement) when the others are known. Typically, the properties of a surface are probed using water as a probe liquid. The most comprehensive quantity about a surface is its surface free energy, γ_{SV}. It cannot be directly measured, yet if γ is known (or measured beforehand using another technique) the quantity $\gamma_{SV} - \gamma_{SL}$ can be calculated by estimating the contact angle θ. Use of several probe liquids with different surface tensions allows determination of the surface free energy, since γ_{SL} can be eliminated. However, in many cases it is adequate to evaluate the wetting by water. In this case, surface free energy yields no additional benefit when compared to the contact

*Other possible terms include *hygro-*, *amphi-*, *omni-*, *lipo-*, and *lyo-*.[32]
†An exception of "underwater oleophobicity" exists, yet is not dealt here.

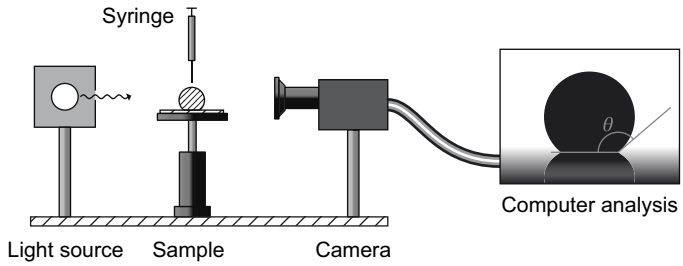

Figure 2.9. Schematic representation of the sessile drop method for measuring contact angle. Not to scale.

angle. The determination of the contact angle is the far most used method for determining surface wettability in the field of superhydrophobicity.

On a surface with fixed parameters (γ_{SV}, γ_{SL}), a drop with a fixed volume adopts a unique shape. Small drops, with diameter less than the capillary length, $2R < \lambda_c$, form a spherical cap shape. This is easy to understand through the Young–Laplace equation (2.1), which states that curvature of surface is directly proportional to the pressure inside the drop. When gravity is neglected, the pressure inside the drop is constant, which results in constant curvature. In principle, a small drop with fixed volume could be uniquely identified by its width:

$$w = \begin{cases} \left[\dfrac{24V}{\pi\left(x^3 - 3x + 2\right)}\right]^{\frac{1}{3}}, & \text{if } \theta \geq 90° \\ \left[\dfrac{24V}{\pi\left(x^3 - 3x + 2\right)}\right]^{\frac{1}{3}} \sqrt{1 - x^2}, & \text{if } \theta < 90° \end{cases} \tag{2.25}$$

However, the exact determination of the volume without resorting to measuring the drop width is difficult. Therefore, often the contact angle is optically determined using a goniometer and the volume of the drop is calculated from its geometric parameters.

The most common method for measuring contact angles is the *sessile drop* method, which is also known as the goniometer method. Therein the studied surface is placed horizontally on a platform and a drop of water is placed onto it by using a microliter syringe. The profile of the drop is recorded with a camera and the images are analyzed with a computer. In this method the contact angle is actually measured at the contact line. The simplest method is known as tangent method, where a straight line is fitted along the perimeter of the drop to assess the contact angle. A slightly more advanced method is to fit a polynomial along the lower part of the drop. Further improvements can be made through fitting a sphere or an ellipse to the whole drop. This method works well for either small drops (diameter much smaller than the capillary length) or hydrophilic surfaces, where the effects of gravity are less significant. The

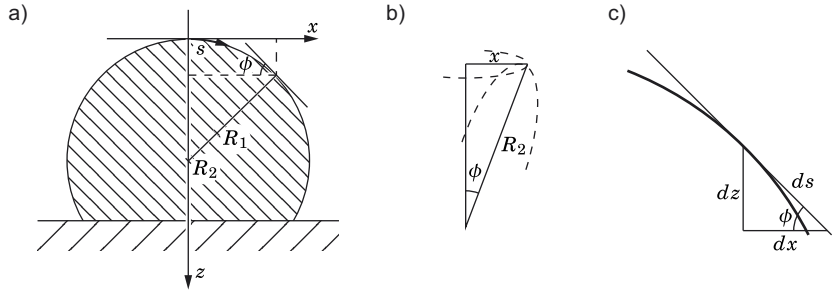

Figure 2.10. The geometry used in deriving the Young–Laplace -shape of a drop in the axisymmetric case. a) s is the path length from top, ϕ is the angle from the vertical axis, R_1 and R_2 are the principal radii of curvature. b) R_2 forms a right triangle with x at angle ϕ. c) The differential steps dz and dx relate to ds through angle ϕ.

definitive method for determining contact angles is to fit a full axisymmetric drop profile based on the Young–Laplace equation (2.1).

Axisymmetric drop-shape analysis (ADSA) yields the most accurate and physically relevant results in sessile drop contact angle analysis.[76,77] Consider a system shown in Figure 2.10, where a drop lies on a surface. Young–Laplace equation states that the pressure difference across the water–air interface is equal to $\Delta p = \gamma C$, where $C = \frac{1}{R_1} + \frac{1}{R_2}$ is the curvature of the surface. The z-axis is drawn downwards from the top of the drop and the x-axis represents the distance from the z-axis. The radii of curvature are rewritten with the help of geometrical considerations (see Figure 2.10b,c):

$$ds = R_1 d\phi \Leftrightarrow \frac{1}{R_1} = \frac{d\phi}{ds}, \tag{2.26}$$

$$\sin\phi = \frac{x}{R_2} \Leftrightarrow \frac{1}{R_2} = \frac{\sin\phi}{x}. \tag{2.27}$$

Hydrostatic pressure, $\Delta\rho g z$, acts on the drop, yet at the top it is zero, which leads to:

$$\frac{1}{R_1} = \frac{1}{R_2} = \frac{1}{R_0} = b, \tag{2.28}$$

$$\gamma\left(\frac{1}{R_1} + \frac{1}{R_2}\right) = \gamma\frac{2}{R_0} = 2b\gamma = \Delta p_0. \tag{2.29}$$

At heights, $z > 0$, hydrostatic pressure is taken into account by writing:

$$\Delta p(z) = \Delta p_0 + \Delta p_g(z) = 2b\gamma + \Delta\rho g z \tag{2.30}$$

$$\Rightarrow \frac{d\phi}{ds} = 2b + \kappa z - \frac{\sin\phi}{x}, \tag{2.31}$$

where the capillary length, $\kappa^{-1} = \lambda_c = \frac{\gamma}{\Delta\rho g}$, was employed. A set of differential

equations can now be written with the help of geometrical identities:

$$\begin{cases} \dfrac{d\phi}{ds} = 2b + \kappa z - \dfrac{\sin\phi}{x} \\ \dfrac{dx}{ds} = \cos\phi \\ \dfrac{dz}{ds} = \sin\phi \end{cases} \tag{2.32}$$

Using s as the free parameter, at the top of the drop, $s = 0$, which leads to $x(0) = z(0) = 0$ and $\frac{d\phi}{ds} = b$. No general solution exists for this set, yet numerical integration readily yields the axisymmetric drop profile.

Sessile drop contact angle analysis typically employes a computer software, which calculates ADSA profiles for different drop sizes and then tries to fit the calculated profile to the photographed drop shape. However, the equations also yield theoretical information about drop shapes and what kind of effects occur with a given set of rules. This approach was employed in Publication I, where numerous drop shapes were calculated to gain insight into the phenomena occurring during contact angle measurements.

2.6.1 The Receding Contact Angle

Publication I considers the difficulties of measuring the receding contact angle using the sessile drop method. Section 2.4 described how the advancing and receding contact angles are defined and also in which way they can be measured. It turns out that measuring the advancing contact angle is facile, yet measuring the receding contact angle often leads to problems. This study found that the reasons behind these phenomena are due to contact angle hysteresis combined with geometry. To comprehend the situation, it is necessary to create a model experiment.

The model defines a simple set of rules:

1. Three parameters define a drop:
   (a) volume, V
   (b) baseline length, L
   (c) contact angle, θ
2. When two are known, the third can be calculated
3. θ is bound by the advancing and receding contact angles, $\theta \in [\theta_R, \theta_A]$
4. When V is increased:
   (a) If $\theta < \theta_A$, increase θ while keeping L constant
   (b) If $\theta > \theta_A$ after previous step, set $\theta = \theta_A$ and increase L
   (c) If $\theta = \theta_A$, increase L while keeping θ constant

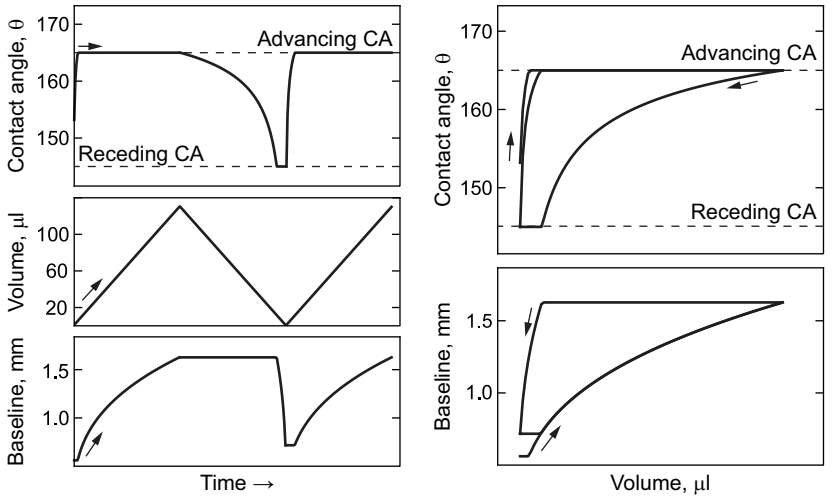

Figure 2.11. Simulated contact angle measurement using spherical-cap approximation. Dashed lines mark the advancing and receding contact angles. The advancing value is quickly reached, yet acquiring the receding value consumes more time.

5. When V is decreased:
   (a) If $\theta > \theta_R$, decrease θ while keeping L constant
   (b) If $\theta < \theta_R$ after previous step, set $\theta = \theta_R$ and decrease L
   (c) If $\theta = \theta_R$, decrease L while keeping θ constant

These rules allow to simulate the measurement of advancing and receding contact angles. An example simulation using spherical-cap approximation is shown in Figure 2.11. Therein volume is increased and decreased using a constant rate. From the starting point, the contact angle reaches the advancing values quickly and saturates. Receding angle is also reached, yet only at a small volume. This behavior was later confirmed also experimentally, which is discussed in Chapter 3. However, simple rules for the volumes needed to reach the advancing and receding contact angles, can be derived.

The volume of a spherical cap is given by Equation (2.22) and the diameter of the circle contacting the surface (*i.e.* "baseline") by Equation (2.23). Consider a situation, where $\theta = \theta_A$ and volume of drop is V_A. When the drop volume is reduced until $\theta = \theta_R$, the baseline lengths are still equal, $L_A = L_R$, which leads to:

$$L_A^3 = \frac{24V_A}{\pi}\left(x_A^3 - 3x_A + 2\right)^{-1}\left(1 - x_A^2\right)^{\frac{3}{2}} \tag{2.33}$$

$$= \frac{24V_R}{\pi}\left(x_R^3 - 3x_R + 2\right)^{-1}\left(1 - x_R^2\right)^{\frac{3}{2}} = L_R^3 \tag{2.34}$$

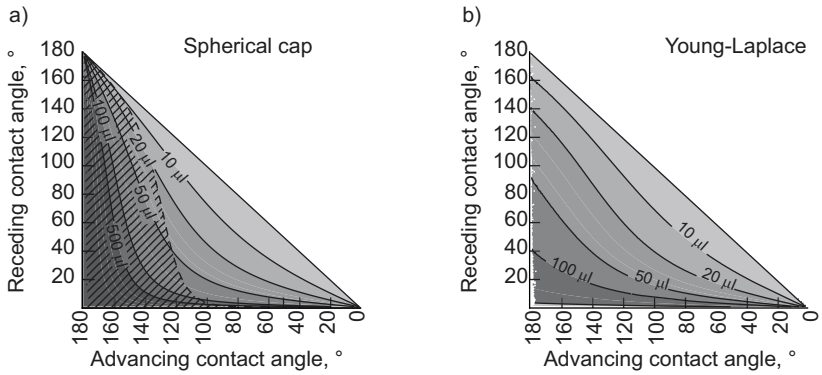

Figure 2.12. Drop volume required to reach receding contact angle at 5 µl. a) Spherical-cap approximation yields acceptable results when either hysteresis is low or the contact angles are less than ~ 120°. Shaded area deviates from Young–Laplace result by more than 50%. b) Result based on solving the Young–Laplace equation yields more accurate results. Adapted with permission from Publication I. Copyright ©2013 American Chemical Society.

resulting in a linear relation:

$$V_{\mathrm{R}} = f(x_{\mathrm{A}}, x_{\mathrm{R}}) V_{\mathrm{A}}, \text{ where} \tag{2.35}$$

$$f(x_{\mathrm{A}}, x_{\mathrm{R}}) = \frac{(x_{\mathrm{R}} - 1)^2 (x_{\mathrm{R}} + 2) \left(1 - x_{\mathrm{R}}^2\right)^{-\frac{3}{2}}}{(x_{\mathrm{A}} - 1)^2 (x_{\mathrm{A}} + 2) \left(1 - x_{\mathrm{A}}^2\right)^{-\frac{3}{2}}} \tag{2.36}$$

These equations yield the volumes required to reach the advancing and receding contact angles at certain volumes. For $\theta_{\mathrm{A}}/\theta_{\mathrm{R}}$ of 150°/100°, the volume when advancing contact angle is reached after residing at receding contact angle at 2 µl, equals 24 µl. In contrast, to reach the receding angle at 5 µl, a volume of 60 µl is required. These results were calculated using the spherical-cap approximation, which exaggerates the volumes, yet still gives qualitative insight. Numerical calculation of the Young–Laplace equation yields more accurate results and, as an example, the required volumes to reach the receding contact angle at 5 µl are plotted as contours in Figure 2.12.

2.7 Wetting Transitions on Hierarchical Surfaces

The leaf of a lotus plant is the most commonly used model superhydrophobic surface. It repels water and keeps itself clean, because water drops gather mud and other particles from the surface while they are rolling off. These remarkable properties are due to the *hierarchical* structure of the plant surface, where papillae of ~ 10 µm are covered with tiny wax tubules.[19] The role of the hierarchical structure is not exactly clear, yet some theoretical considerations show that the hierarchical structures can be more stable than single level structures.

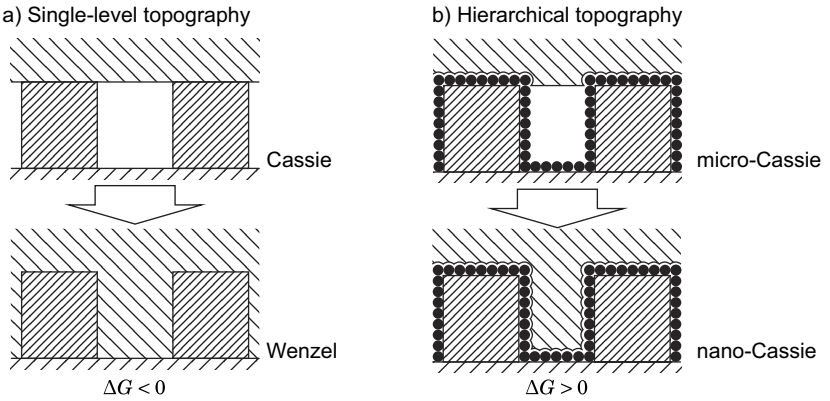

Figure 2.13. Hierarchical wetting demonstrated. a) On single-level topography the transition from the Cassie–Baxter to the Wenzel state is energetically favorable. b) The "micro–Cassie" state on a hierarchically structures surface is energetically favored to the "nano–Cassie" state.

Energetics of wetting transitions of single-level topographies were described in Section 2.3. Equations (2.7) and (2.8) are general for any wetting transition from a composite state to a fully wetting state. Therefore, also Equation (2.10) is of general form. It is necessary to consider in which ways to modify these equations to account for hierarchical surfaces. Young's equation (2.3) describes contact angle on a smooth surface, and both the Cassie–Baxter and Wenzel equations relate the apparent contact angle to the Young's contact angle. In a simple approximation, the small-scale structure can be considered an equivalent smooth surface, as long as no wetting transition alters its wetting properties.

$$\cos\theta = \left(\gamma_{\mathrm{SV}} - \gamma_{\mathrm{SL}}\right)/\gamma \equiv \cos\theta^{\star}_{\text{s-s}}, \text{ and} \tag{2.37}$$

$$\Delta G_{1\to 2} = -\gamma\left(A_{\mathrm{LV}} + A_{\mathrm{SV}}\cos\theta^{\star}_{\text{s-s}}\right), \tag{2.38}$$

where $\theta^{\star}_{\text{s-s}}$ is the equivalent Young's contact angle of the small-scale structure. A requirement for more stable non-wetting state is that transition from it consumes free energy. Therefore, $\Delta G_{1\to 2} < 0$, which leads to a geometrical constraint:

$$\frac{A_{\mathrm{LV}}}{A_{\mathrm{SV}}} < -\cos\theta^{\star}_{\text{s-s}}, \tag{2.39}$$

which also yields a geometric limit for single-level topographies, for which $\theta^{\star}_{\text{s-s}} \lesssim 120°$, namely $A_{\mathrm{SV}} \gtrsim 2A_{\mathrm{LV}}$. The value states how deep the protrusions need to be compared to the wetted area. Surfaces, which do not satisfy this requirement, can be energetically stable only if they are hierarchically structured. Consider a surface, for which $\theta^{\star}_{\text{s-s}} = 160°$, *i.e.* a hierarchically superhydrophobic surface. In this case the limiting geometry is $A_{\mathrm{SV}} \gtrsim 1.02A_{\mathrm{LV}}$. An upper limit occurs when $\theta^{\star}_{\text{s-s}} = 180°$, which leads to a result that surfaces with $A_{\mathrm{SV}} < A_{\mathrm{LV}}$ cannot

exhibit a stable non-wetting state. In conclusion, hierarchical wetting extends the possible energetically stable geometries to $\frac{A_{LV}}{A_{SV}} \in \left[\frac{1}{2}, 1\right]$. However, this is not the only benefit of a hierarchical surface, yet also the pressure stability is improved.

Equation (2.16), which is universal for wetting structures of similar posts or trenches, gives the force required to move a wetting contact line downwards on a structured surfaces. Consider two surfaces, a single-level topography with $\theta_{A,1} = 120°$ and another with hierarchical topography, $\theta_{A,2} = 170°$. If the critical pressures are written as equal, $\Delta p_{c,1} = \Delta p_{c,2}$, a limit can be derived for the geometrical constraint, namely L/A (see Equation (2.16)):

$$(L/A)_1 \cos\theta_{A,1} = (L/A)_2 \cos\theta_{A,2} \tag{2.40}$$

$$f_{geom} = \frac{(L/A)_2}{(L/A)_1} = \frac{\cos\theta_{A,1}}{\cos\theta_{A,2}} \tag{2.41}$$

and replacing the contact angles, yields $f_{geom} \approx 0.51$, with the lower limit of $f_{geom} = \frac{1}{2}$ at $\theta_A = 180°$. Thus, for the same stability, *i.e.* same critical pressure, the size of the structure (which affects parameter L) can be up to half smaller with the same pitch (which affects parameter A). This results in the fact that hierarchically superhydrophobic structures are more stable in terms of pressure. To get some values, a model structure presented in Section 2.3 can be considered. Therein, $L = 4r_p$ and $A = 3r_p^2$, which leads to $\Delta p \approx 4.8$ kPa for single-level topography ($\theta_A = 120°$) and $\Delta p \approx 9.5$ kPa for hierarchical surfaces ($\theta_A = 170°$).

3. Experimental Results

"No amount of experimentation can ever prove me right;
a single experiment can prove me wrong."
– Albert Einstein

This section describes in detail the synthesis of silicone nanofilaments and the processes to create functionalized nanocellulose aerogels. Furthermore, a model for the formation of silicone nanofilaments is proposed. The chosen method for contact angle measurements is also briefly discussed.

3.1 Silicone Nanofilaments

Silicone nanofilaments (SNFs) are a novel class of materials, which were independently introduced by three research groups during 2006–2007.[78–80] They comprise superhydrophobic surfaces, whose fabrication method is facile and which have also been found to exhibit good mechanical and chemical stability[81,82] as well as scalability of production.[83] As shown in Figure 3.1, a surface with a percolating network of filaments (*i.e.* fibers) with diameters of 10–100 nm forms the basis of all SNF materials. These filaments are synthesized through either a gas-phase or solvent-phase synthesis onto a hydroxyl-terminated substrate, such as silicon or glass. The most commonly used precursor molecule is *methyltrichlorosilane* (MTCS), which has three reactive Si–Cl bonds along with a methyl group, which provides intrinsic hydrophobicity. Instead of chlorine, the reactive group can also be methoxy, ethoxy, or even dimethylamino, yet they typically require a catalyst, such as HCl.[84] Remarkably, SNF surfaces created by solvent-phase synthesis onto silicon wafers have been reported to exhibit perfectly hydrophobic (PHO) water contact angles of $\theta_A/\theta_R = 180°/180°$,[79,84] yet typically the surfaces exhibit advancing contact angles up to *ca.* 170° with hysteresis $\Delta\theta_{\%} \lesssim 10\%$.[78,81–83,85–90]

Figure 3.1 depicts a typical morphology of SNF-coated surfaces. The filaments form a densely packed surface with sub-micron features. The individual nanofilaments are hydrophobic because their exteriors are mostly covered by methyl groups, which provide low surface energy. Therefore, a drop in contact with such a nano-rough hydrophobic layer, experiences wetting governed

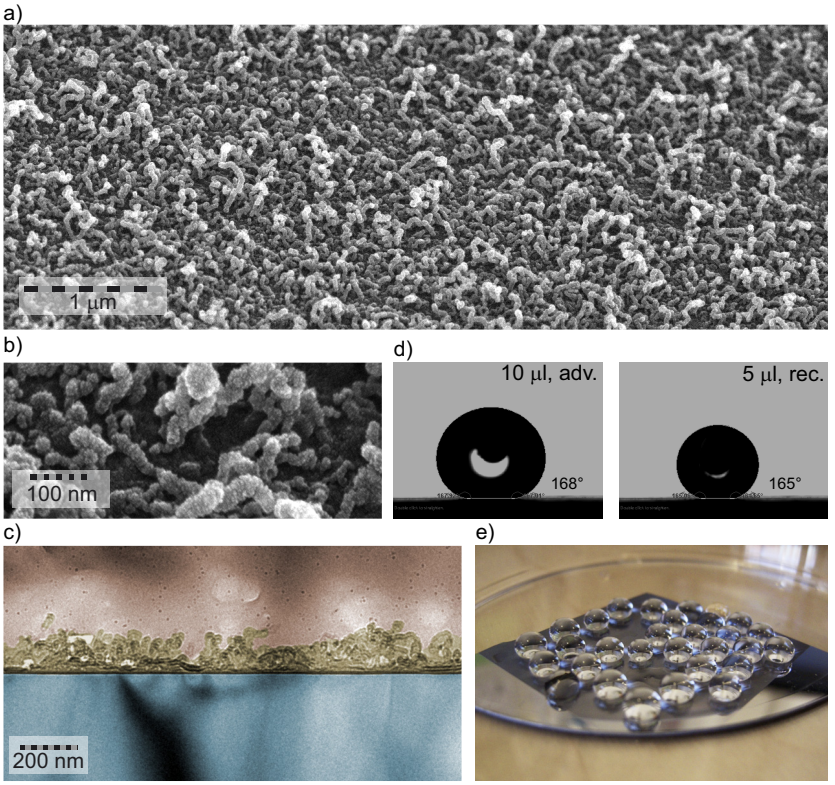

Figure 3.1. Silicone nanofilaments. a) A tilted scanning electron micrograph of a typical SNF surface. b) A higher magnification scanning electron micrograph. c) *Color added for emphasis.* A cross-sectional transmission electron micrograph of SNFs. d) Photographs from contact angle measurement show θ_A/θ_R = 168°/165°. e) A photograph of water drops on a hierarchically superhydrophobic SNF surface.

by the Cassie–Baxter equation (2.6). A surface coated with SNFs is difficult to wet, because of the high intrinsic contact angle of the nanofilaments. This leads to a trapped air layer beneath the filaments, which accounts for the superhydrophobicity. The fraction of water actually in contact with the filaments can be low, which also reduces the hysteresis,[91] since the filaments act as "hydrophilic pinning sites" on a surface of air.

3.1.1 Synthesis of Silicone Nanofilaments

The synthesis of SNFs is based on the properties of the silane precursor molecule, which is typically methyltrichlorosilane. It comprises three reactive groups, which is essential for the formation of the structures. Methyltrichlorosilane leads to a monolayer, dimethyldichlorosilane forms silicone "loops", and tetrachlorosilane creates structures, such as spheres or films. However, a mixture of mono-functional and tetra-functional silanes can also lead to SNFs.[87] See Figure 3.2 for a schematic representation of the reaction process. In the reac-

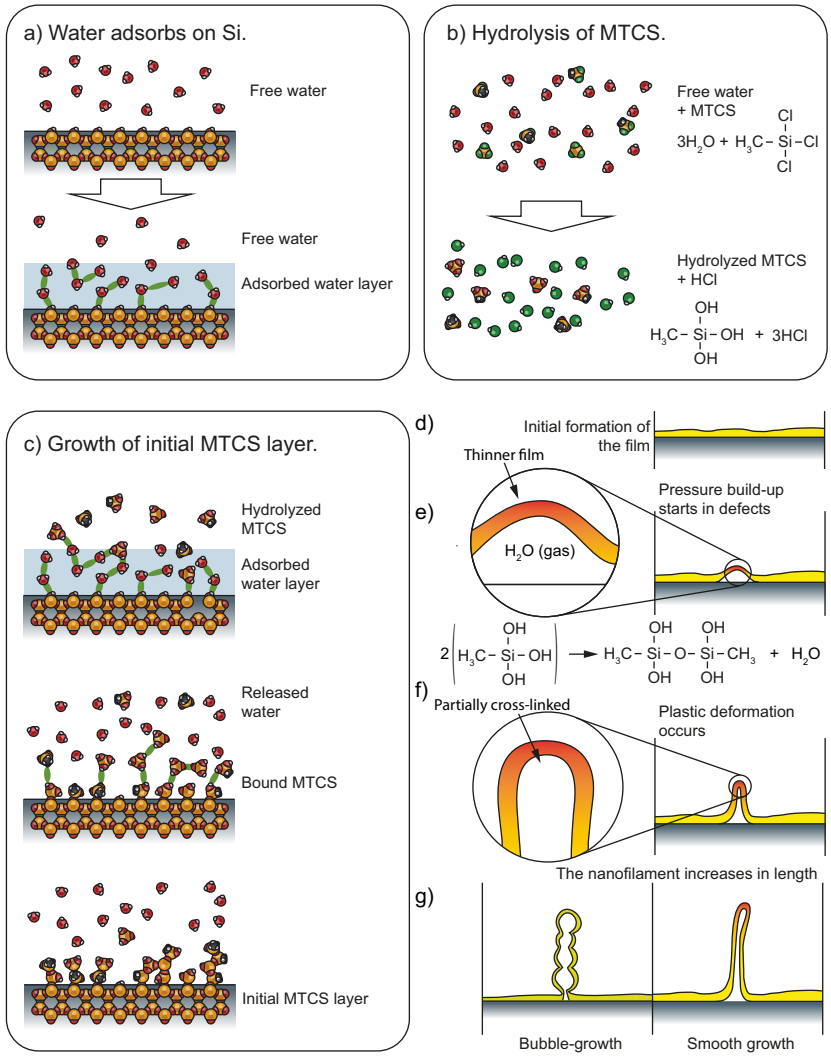

Figure 3.2. The formation mechanism of silicone nanofilaments. a) First, water adsorbs onto the substrate. b) MTCS is fully hydrolyzed before it reaches the substrate. c) The hydrolyzed MTCS molecules physisorb onto the water layer and finally chemically bond to the substrate. d) A thin continuous film is formed. e) A pressure pocket is created at a defect site, while water vapor is generated through the cross-linking reactions. f) The pressure inside the defect increases, which causes elongation of the film towards the tip of the defect. g) A nanofilament is formed through continuous or sequential expansion of the defect site.

tion, water from the surrounding fluid first adsorbs onto the substrate surface (Figure 3.2a). This is an extremely important step as either too high or too low water contact will prevent the creation of the filaments. The second process is the hydrolysis of the silane species, where *e.g.* MTCS hydrolyzes into methylsilanetriol (h-MTCS) in the fluid phase, *i.e.* before reaching the substrate (Figure 3.2b). Also other precursor molecules follow the same reaction pathway, which is the reason behind only MTCS being considered here. Third, h-MTCS physisorbs to the adsorbed water layer and starts to cross-link with each other and the substrate (Figure 3.2c). The water molecules might act as catalysts in the process. The thickness of the initial water layer is an important factor. An initial film or separate islands of partially cross-linked silanes form onto the substrate. After this point, different authors suggest different pathways towards the silicone nanofilaments.[84,86,87,92]

Gao and McCarthy[87] created SNFs from a chlorotrimethylsilane/tetrachlorosilane (CTMS/TCS) azeotrope (*i.e.* a mixture whose components boil simultaneously). Their model is based on CTMS species acting as terminating agents for the three-dimensional growth of TCS structures. The CTMS/TCS ratio was 1:10. They envision that TCS reacts with water and polymerizes while CTMS molecules terminate the growth. These entities should form particles, whose surface is mostly covered with un-reactive methyl groups. However, the growth could continue from defects on the surface, which accounts for the loss of symmetry in the system. To enable continuous growth, the terminating CTMS species should selectively attach to the sides of the forming filaments while TCS forms the core. The weakest point in this growth model is the explanation for the loss of symmetry and the model only explains the growth when there are terminating molecules available. Therefore, it is not a model that can be considered generally valid for SNFs synthesized from MTCS.

Rollings and Veinot[92] introduced a more in-depth model for the growth of SNFs from vinyltrichlorosilane (VTCS), which is basically similar to MTCS with the difference that it is not extremely hydrophobic due to the vinyl groups. However, they could render their SNFs more hydrophobic by further passivating them with a fluorosilane, which attaches to the vinyl groups at the surface. Their growth model starts from the attachment of VTCS to the surface. All three reactive groups cannot simultaneously attach to the reactive sites at the substrate, which leaves one or two of them dangling from the surface. They state that when two of the VTCS species cross-link, the vinyl groups need to arrange themselves away from each other, which creates a suitable direction for the continuation of the growth. Condensation of VTCS molecules create is-

lands on the surface, which creates a favorable site for further condensation, since they are "closer" to the vapor phase. However, if this was the case, the diameter of the filaments would be dictated by the chemistry of the silane species alone. It would seem to suggest a diameter of only a few molecules for the filaments, while observations indicate diameters up to > 50 nm. The study presents no limiting mechanism, which would prevent the creation of continuous films during the island growth phase. Furthermore, the loss of symmetry is vaguely argumented. Especially the reasons behind the inhibition of three-dimensional growth after the island formation remains unclear.

Khoo and Tseng[86] suggested an amphiphilic "self-assembly" -type mechanism for the growth of the filaments from MTCS. Therein the hydrophobic species would orient themselves away from the core of the filament, which is more hydrophilic. However, the driving forces for such short molecules are most likely negligible in the time scale of the reaction, which they also note themselves. In addition, the most important step, namely the formation of the initial filaments, is neglected. Thus, no explanation for the break of symmetry is presented. It is only briefly mentioned that methyl groups might preferentially align themselves at the perimeter of the filaments, which would lead to the inhibition of lateral growth.

Chen *et al.*[84] presented important data, which indicate that their SNFs consist of $CH_3SiO_{1.12}(OH)_{0.76}$. Thus, *ca.* three quarters of the silanes are only partially cross-linked. They did not observe any chlorine in the end-product, which indicates that the molecules were readily hydrolyzed. The study envisioned that $CH_3SiO_{1.5}$ species bind with three $CH_3SiO(OH)$ species to form a secondary building unit, which in turn can polymerize into linear structures. These structures can further aggregate into filament-like morphologies. Their model is draw in plane, while the molecules are in reality tetragonal. This creates inconsistencies together with the assumption that the molecules and bonds are rigid. Furthermore, no limiting mechanism is given for the lateral growth and thus the break of symmetry is inadequately explained.

Apparently, all the presented models could be improved and especially the break of symmetry is inadequately covered. Publication II presents a viable growth model, which also explains the break of symmetry using purely physicochemical and kinetic arguments. The model is given below, in Section 3.1.3, after the description of the synthesis setup used.

3.1.2 Gas-Phase Synthesis

SNFs have been synthesized using three distinct pathways: *solution-phase*, *atmospheric gas-phase*, and *vacuum gas-phase* methods. In solution-phase synthesis, a substrate is immersed into an inert anhydrous solvent, such as toluene, followed by injection of the silane precursor.

Publication II describes a vacuum gas-phase synthesis apparatus used to synthesize SNFs, which is schematically presented in Figure 3.3. The reactor vessel comprised a glass container closed with a lid, which was sealed with an O-ring coated by a fluoropolymer and silicone-based high vacuum grease. Inlet stopcocks were made from PTFE (*i.e.* "Teflon"). Inlet tubings consisted of either PTFE or silicone, which were found to be sufficiently inert, although silicone hardened with time and had to be regularly replaced. Vacuum and exhaust tubings were either PVC or stainless steel. Sealing of inlet connections was performed using PTFE collars and high vacuum grease. Thus, the materials directly in contact with the reaction were limited to glass, PTFE, and a trace amount of high vacuum grease.

A typical SNF synthesis procedure followed these steps. Substrates were either microscopy glass slides, or more typically 100 mm diameter test grade Si <100> wafers (Universitywafer, South Boston, U.S.A), which were cut into quarters of *ca.* 2000 mm^2 area. Substrates were ultrasonicated in a heated bath (60 °C) of mild alkaline detergent (10% vol./vol., Deconex 11 Universal, Borer Chemie, Switzerland) for 15 minutes, thoroughly rinsed with de-ionized water (> 20 $M\Omega m^{-1}$, Milli-Q, Millipore, U.S.A.), and dried under a stream of nitrogen. Further surface activation was performed by plasma treatment (O_2/H_2, Gatan Solarus Model 950, plasma power 60 W) for 15 minutes to increase the surface hydroxyl coverage. After the activation, the substrates were stored in plastic containers and promptly used.

The substrate was transferred onto a flat PTFE substrate holder inside the reactor vessel shown in Figure 3.3, after which the reactor was sealed and evacuated to *ca.* < 1 mbar. The reactor vessel featured a double-wall structure, where a heating fluid could be circulated. However, creating a homogeneous temperature inside the reactor proved difficult due to the poor heat transfer between the lid and the reactor, which was further hindered by the presence of vacuum. Therefore, the reactions were run at room temperature, which was *ca.* 20–23 °C. The reactor was evacuated for roughly 30 minutes, after which the desired volume of deionized water was pipetted into a test tube, which was then connected to the reactor, where the water evaporated with the help of some ex-

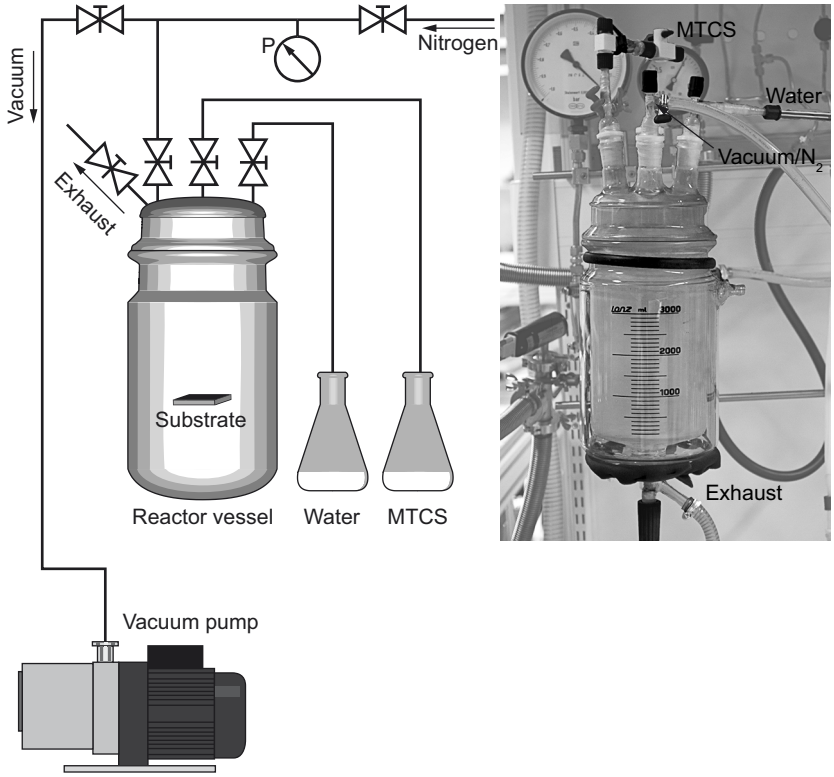

Figure 3.3. Silicone nanofilament synthesis apparatus. Water and silane precursor (MTCS) are injected through separate inlets to ensure that mixing occurs inside the reactor and tubing is kept short to eliminate dead volume. A metallic sealing clamp connecting the reactor vessel to the lid is not shown in the photograph.

ternal heating by a hot air blower. The inlet was again closed and the system was let to equilibrate typically for 15 minutes. The wanted amount of MTCS was measured into a PTFE container with a valve, which allowed sealing the liquid inside an inert environment. The handling of MTCS was done exclusively under nitrogen atmosphere. The valve was connected to the reactor inlet and both valves opened. MTCS evaporated readily and diffused into the reaction chamber, where the synthesis occurs. The MTCS inlet valve was left open until the end of the reaction, which lasted from 15 minutes to more than 12 hours. Typically, the reaction was run over night. Finally, the reactor was flushed with a dry nitrogen stream at atmospheric pressure. Flushing duration was *ca.* 30 minutes to allow the removal of unreacted species and reaction by-products, such as HCl.

3.1.3 Proposed Growth Model

To explain the reasons behind the forthcoming model, it is vital to shortly describe which observations lead to this proposition. First, transmission electron

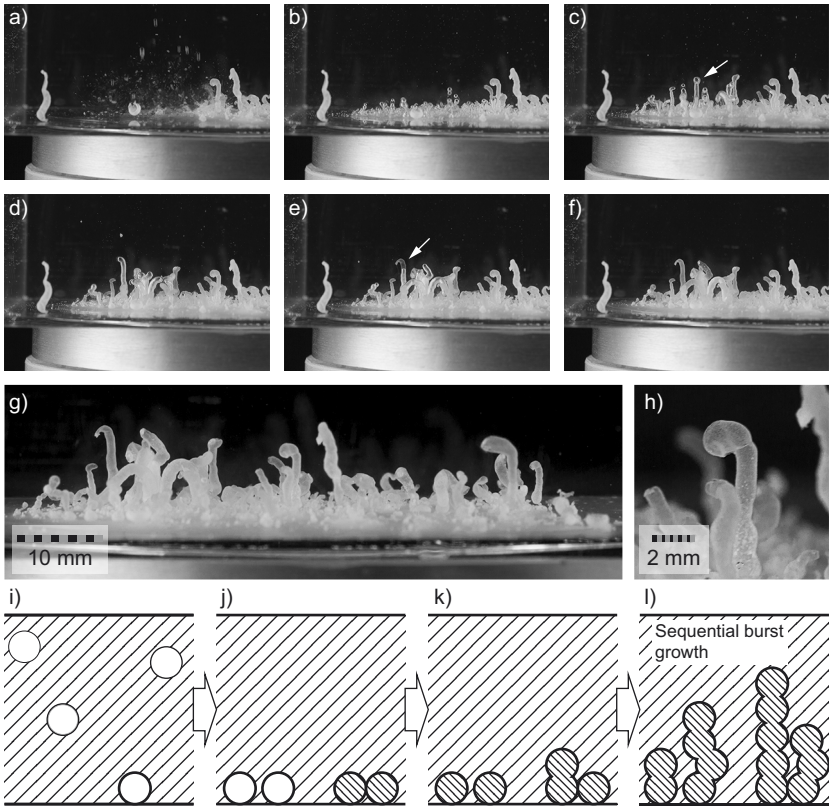

Figure 3.4. The growth of silicone *macrofilaments* under water. A sequence of photographs showing a) the initial shell polymerization, b–d) bubble-burst growth e–f), and that finally the filaments fill with water. g) A silicone macrofilaments "forest". h) A close-up of a single macrofilaments. i)–l) A schematic representation of the growth process, where shells first polymerize and then sequentially burst to release more material into the water phase.

microscopy revealed *hollow* filaments, which are shown in Figure 3.1c. Not all of the observed SNFs were hollow, yet enough to dismiss the possibility of imaging artifacts. The creation of hollow nano-structures clearly contradicts the previously proposed growth models. Second revelation came when disposing of out-dated MTCS by pouring it into a bath of water. Drops of MTCS quickly turned white in the water and fell to the bottom of the container. However, it was only the beginning. The "pearls" rapidly burst and created "pearl-necklace" -type structures, which greatly resembled SNFs, while being at the millimeter-scale. These *macrofilaments* might be generated through a process similar to SNFs.

Photographs of silicone macrofilaments are shown in Figure 3.4 along with a schematic representation the growth process. First, drops of MTCS were injected into the water phase using a syringe. The drop shell quickly polymerized in contact with water and the drop fell to the bottom of the container. Hydrolysis and cross-linking of the MTCS species continued inside the shell, which

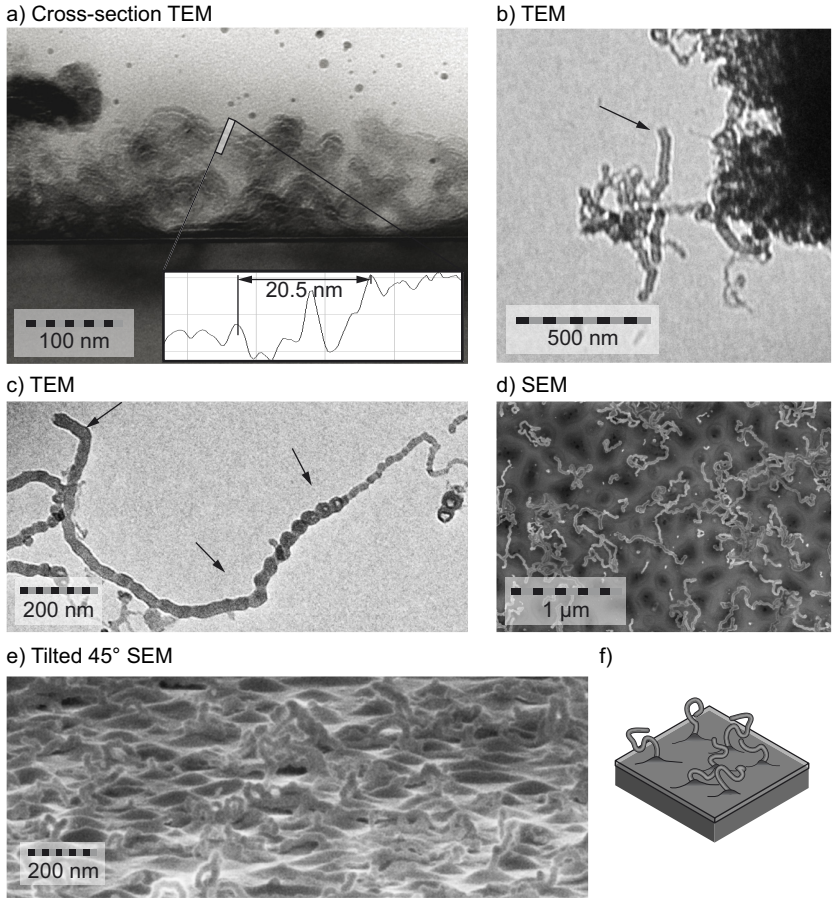

Figure 3.5. Silicone nanofilaments and hollow structures. a) A cross-section transmission electron micrograph shows that the SNFs exhibit a hollow core. The width of a SNF equals *ca.* 20.5 nm. b) Transmission electron micrograph of a SNF, which has been mechanically cleaved, displays a hollow core. c) Continuous and bubble-burst growth modes demonstrated on a single SNF. The onset locations are marked with arrows. d) Scanning electron micrograph of a SNF surface, which exhibits a rough layer behind a sparse coverage of SNFs. e) Tilted scanning electron micrograph exhibits partially grown SNFs originating from protrusions. f) Schematic representation of SNFs on a surface.

caused a rapid pressure increase inside the drop as water vapor was continuously generated. The shell burst from the top and released liquid MTCS into the water phase, which in turn polymerized to a new shell. The growth continued either by bubble-burst sequence or continuously (Figure 3.4c). Finally, when all of MTCS was consumed, only a thin shell remained, which then filled with water (Figure 3.4e). A close up of a macrofilament (Figure 3.4h) shows that its shape remarkably resembles SNFs.

The growth of the initial layer of silane has been well covered by Rollings and Veinot.[92] The proposed growth model starts from this initial layer, which generates connected islands or “mountains”. The previous models have expected that directional growth occurs directly from these mountains, typically due to

some kind of arrangement of methyls to the outside edges, but not to the top where the growth continues from. The current model aims to explain exactly this phase of the process, see Figure 3.2. When the initial film forms, it is incompletely cross-linked, yet the chemical reactions continue inside the film. This generates H_2O vapor inside the film, which concentrates into defects in the film. Pressure rises inside the defects, which causes the films to expand upwards. The incompletely cross-linked film is not fully elastic, yet it might also exhibit plastic deformation. At a certain pressure, the stress in the film becomes large enough to reach the point where plastic yield occurs. When the film expands, it exposes more unreacted sites, which can bind with incoming MTCS molecules. The tip of the structure is the point where the film is most likely to expand from to accommodate for the increasing pressure. Therefore, it is the location where the break of symmetry in the system occurs. Because the process generates gases inside the film, the interior of the filament may be left hollow, providing it does not collapse or fill-up at a later stage. Also, depending on the rate of expansion and gas generation, the expansion of the filament can be either continuous or it can occur by a bubble-burst mechanism.

Figure 3.5 displays cross-sectional transmission electron micrographs, where a hollow core is visible inside an SNF. A hollow core is explained by the pressure pocket forming inside the film as the nanofilaments grow, which is in analogy with the growth mechanism of the macrofilaments. A further implication of the growth model is that the observed structure should be dependent on the kinetics of the reactor system. The optimal reaction parameters appear to be reactor dependent and thus it is difficult to assess general guidelines for the growth. Parameters affecting the system are at least fluid medium (air, vacuum, solvent), reactor size, concentrations of water and silane, substrate size, and reactor temperature. Luckily, a wide range of parameters allow the synthesis of SNFs, yet the optimization of the reaction can prove challenging.

3.2 Hierarchically Superhydrophobic Surfaces

Section 2.7 presented some benefits for creating hierarchically superhydrophobic surfaces compared to single-level topographies, namely better stability of the highly non-wetting state and the possibility for a reverse transition due to energetics of the transitions. Here, two approaches were combined to create hierarchically superhydrophobic surfaces: traditional silicon lithography and silicone nanofilaments. Microposts of 10 µm diameter, and 20 µm pitch were fabricated on Si <100> wafers by UV lithography on a photoresist followed

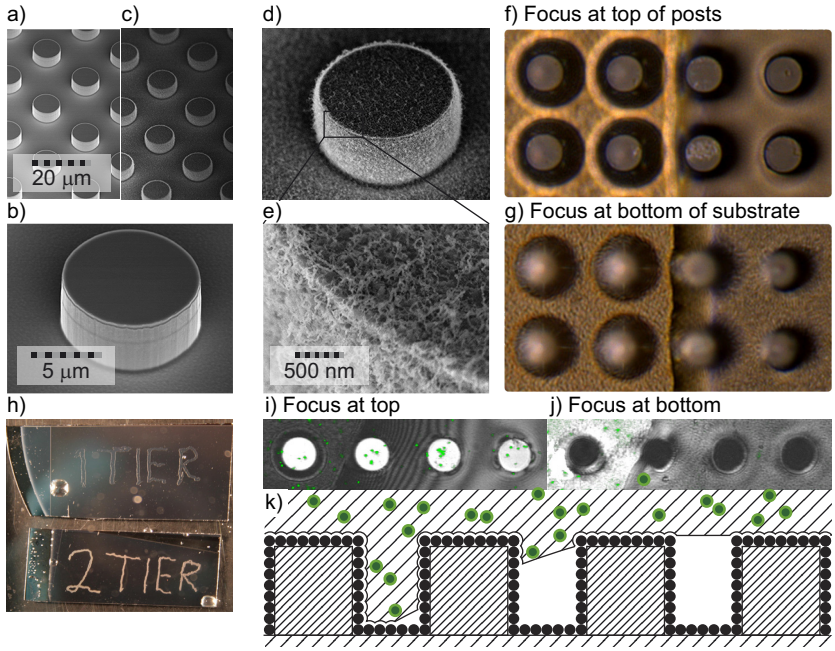

Figure 3.6. Hierarchically superhydrophobic silicone nanofilament surface. Scanning electron micrographs of: a) silicon microposts, height 5 µm; b) close-up of a single post; c) microposts covered with silicone nanofilaments; d) close-up of a single nanofilament-coated post; e) close-up of the silicone nanofilaments. f)–g) Optical micrographs of a transition line from micro-Cassie (right) to nano-Cassie (left). h) A photograph of immersed single-level ("1 tier") and hierarchical ("2 tier") surfaces with pressure induced wetting transitions. i)–j) Scanning laser confocal microscope images from a transition line. Green dots are nanoparticles, which reside in the water phase. k) A schematic representation of the nanoparticles inside water.

by cryogenic deep reactive ion etching (Oxford Instruments, PlasmaLab 100). Gas-phase reaction method synthesized silicone nanofilaments on the micro-patterned surfaces after activation by O_2/H_2 plasma (Gatan Solarus, Model 950). Figure 3.6 shows that the posts were fully covered with silicone nanofilaments.

The hierarchically superhydrophobic micropost/SNF surface exhibited two wetting states called "micro-Cassie" and "nano-Cassie" based on the size of the non-wetting topography. The micro-Cassie resembled the traditional Cassie–Baxter wetting state, where the air–water interface lies above the posts. In the nano-Cassie state, the interface protruded between the microstructures, yet did not wet the SNF layer, which remained in a superhydrophobic state. Confocal microscopy and optical microscopy revealed information about the surfaces immersed in water, where a trapped air layer (*i.e.* "plastron") resided. Using a jet of water from a syringe, it was possible to switch from the micro-Cassie state to the nano-Cassie state, simply by inducing a local overpressure on the structure (Figure 3.6h). The nano-Cassie state was more reflective than the Wenzel state on a single-level topography, which was due to light reflecting from the

plastron. Reversely, a nano-Cassie to micro-Cassie transition could be induced by sucking water slightly above the surface. A confocal microscopy technique employing fluorescent nanoparticles in the water phase revealed the shape of the water–air interface together with interference fringes, which yielded information about the curvature of the plastron at the interface (Figure 3.6i–k). Only recently, studies have successfully attained reversible wetting transitions, which have been mostly achieved by electric-induced processes or physical disturbances.[93–99]

3.2.1 Atomic Layer Deposition

Atomic layer deposition (ALD) is a thin film deposition technique, where typically inorganic materials, such as oxides, deposit on a surface in a step-wise, self-limiting manner.[100,101] ALD is often considered a subcategory of chemical vapor deposition (CVD), where the precursor molecules are simultaneously introduced into the reaction chamber. The benefits of ALD when compared to CVD include sub-monolayer control of film thickness, uniform coatings on three-dimensional substrates, surface-limited reactions, and lower reaction temperatures. In 1970s Finland, Suntola *et al.* introduced ALD for the manufacturing of electroluminescent displays,[102,103] yet already in 1966 researchers in the Soviet Union had been developing a similar method for the deposition of SiO_2.[104] Nowadays, ALD is an extremely interesting research tool and it is also used commercially, for example, to produce high-k -dielectrics in microelectronic chips[106,107] and also as a corrosion protection layer for silver in jewelry.[108]

Simplified, an ALD reactor comprises a reaction chamber, where the substrate is placed, inlets for precursor molecules and an outlet for flushing. The reaction chamber is in vacuum and the substrate is heated typically to 100–300 °C. At first, an inert gas, such as nitrogen, transports the first precursor to the chamber, where it reacts with the surface to form a uniform layer. The substrate temperature is an important parameter, which has to be selected such that multilayer condensation is inhibited, yet the rate of deposition vs. evaporation is low enough to allow good coverage. The temperature range between these two extremes is called the “ALD window”. It refers to the region where the growth is surface limited and does not depend strongly on pulse times or the actual temperature. Next, the inert gas purges away the unreacted molecules as well as the reaction byproducts. Then the second precursor molecule is introduced and the process is repeated until the desired amount of bi-layers are created.

A typical ALD cycle for depositing aluminum oxide consists of a trimethylaluminum (TMA) pulse, purge, a water pulse, and a final purge. The pulse and purge times depend on the reactor geometry and the topography of the substrate. While for planar substrates sub-second pulse times are often adequate, complex three-dimensional materials may require pulse times up to several minutes. In the TMA/water process, TMA is first released into the reaction chamber. One of the methyls of the TMA molecules reacts with a surface hydroxyl to create an oxygen bridge between the surface and the Al. The reactions by-products and un-reacted species are flushed away with an inert gas. In the next step, water is introduced into the chamber, which results in hydrolysis of the methyls of the dangling TMA molecules, which in turn create new sites for the incoming TMA molecules to bind to in the next cycle. Lastly, the chamber is purged. The process continues and creates a well-controlled layer of Al_2O_3. Many other ALD processes follow the same principles as the model described above.

3.3 Nanocellulose

Cellulose is an abundant biopolymer found, for example, in the polysaccharide wall of plant cells.[109] Depending on the context, cellulose can refer to either the cellulose molecules themselves; to nanofibrils, which comprise a pack of chains of cellulose molecules; or to bundles of nanofibrils. This study concerns mostly cellulose nanofibrils,* which are typically 3–15 nm in diameter and can be up to several micrometers in length. Often these nanofibrils pack into larger bundles of several tens of nanometers in diameter. Materials which are composed of cellulose nanofibrils are here denoted as “nanocellulose”. Nanocellulose typically also contains hemicelluloses and other impurities, yet these are not considered here. Mechanical or enzymatic cleaving of pulp using various methods, such as high pressure homogenization and mechanical grinding together with enzymatic or chemical pretreatment, such as TEMPO-oxidization, can be employed to manufacture nanocellulose hydrogels,[110–116] examples of which are depicted in Figure 3.7. The hydrogels comprise a percolating network of cellulose nanofibrils. In this study, the context of nanocellulose is strictly limited to being a physical template for further functionalization and the intrinsic properties of the material have deliberately been left out of the scope.

*also denoted as microfibrillated cellulose, nanofibrillated cellulose, cellulose microfibrils, or nanocellulose fibrils

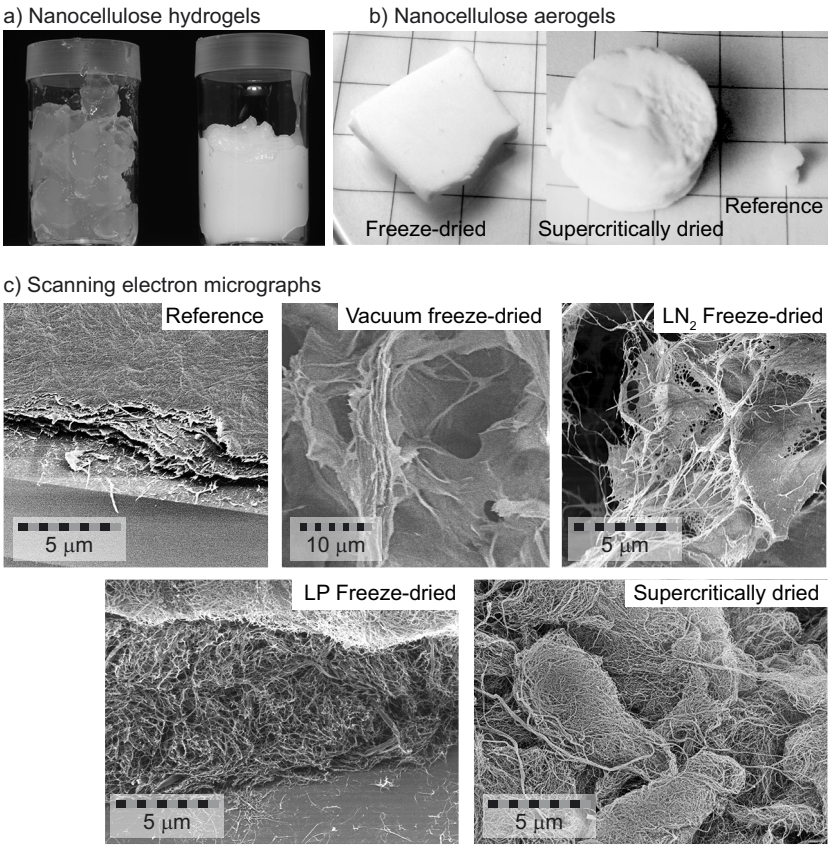

Figure 3.7. Nanocellulose hydrogels and aerogels. a) A photograph of two batches of nanofibrillated hydrogels. The one of the left has been chemically pretreated (TEMPO-oxidization) and high-pressure homogenized, and the one on the right has been mechanically ground. b) Photographs of dried nanocellulose aerogels. Reference sample was dried in ambient conditions, yet it had the same wet volume as the aerogels. c) Scanning electron micrographs of the aerogels with different drying methods. Adapted with permission in part from Publications IV and V. Copyright ©2011 American Chemical Society.

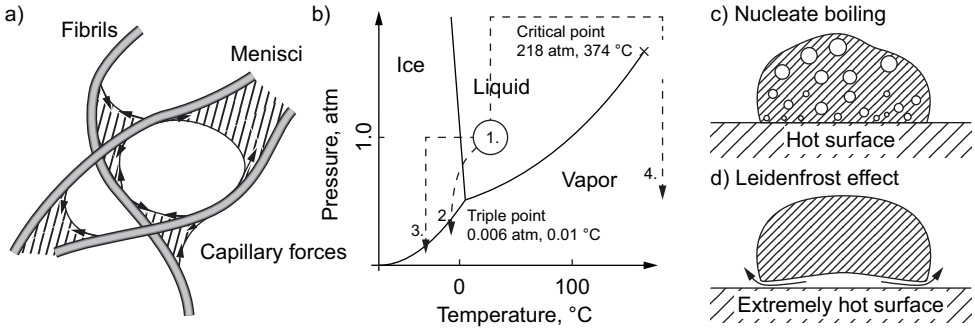

Figure 3.8. Water menisci between fibrils, water phase diagram, and Leidenfrost effect. a) Water menisci form as bridges between fibrils during drying. A capillary force acts to pull the fibrils together as shown by the arrows. b) Phase diagram of water displays routes from liquid phase to gas, *i.e.* drying. **1. Ambient drying.** Drying in ambient conditions leads to collapse due to liquid–to–vapor phase transition. **2. Vacuum freeze-drying.** Adiabatic decrease in pressure leads to freezing of water before reaching the liquid–to–vapor boundary, which suppresses the collapse of fibrils. **3. Cryogenic freeze-drying.** Plunging the hydrogel into liquid nitrogen or liquid propane leads to rapid freezing of water. Subsequent vacuum drying leads to no collapse. **4. Supercritical drying.** In supercritical drying the phase transition to vapor is suppressed completely by going around the critical point. For water, the critical point exists at an inconveniently high pressure and temperature. Therefore, typically CO_2 (critical point *ca.* 31 °C, 73 atm) is employed instead. c) A drop of water on a hot surface typically experiences nucleate boiling, which results in rapid evaporation. d) On an extremely hot surface, a drop of water experiences *film boiling*, which results in an insulating layer of gas beneath the drop, *i.e.* the Leidenfrost effect.

3.3.1 Nanocellulose Aerogels

In 1930s, Kistler[117] discovered a novel class of materials called “aerogels”. They comprise percolating networks of solid material (silica) with air as the matrix medium and they were supercritically dried from hydrogels.[118] Already in the 1940s, silica aerogel powders were commercially sold as a filler material for paints,[119] yet it has taken up to the modern age for more complex applications to emerge. Nowadays, aerogels have been used, for example, as thermal insulation for construction and in clothing, acoustic insulation, capacitor dielectrics, additives, and even cosmic dust collection.[120–122]

Drying nanocellulose hydrogels in ambient conditions lead to collapsed fibrillar films, which resembled paper or thin plastics. The collapse was due to capillary forces acting through menisci forming between nanofibrils during the drying phase when a liquid–to–vapor phase transition occurred (see Figure 3.8a). However, careful removal of water without a collapse of the structure could be achieved through freeze-drying or supercritical CO_2-drying from nanocellulose,[123] or from chemically modified or solubilized cellulose.[124–126] These materials are called nanocellulose aerogels, since they consist of an extremely low density network of cellulose nanofibrils. Nanocellulose aerogels have exhibited good mechanical properties[123,127,128] and they have been used for various functionalities, such as photo-switchable absorption,[129] floatation,[88] and magnetic

actuation[126].

3.3.2 Aerogel Drying Methods

Publication IV also compared different drying methods for aerogels, which compliments the research by Pääkkö *et al.*,[123] who compared ambient drying to vacuum freeze-drying and cryogenic freeze-drying in liquid propane. Altogether, four aerogel drying methods can be identified, in addition to drying under ambient environment. Figure 3.7 depicts a summary of the observed morphologies for different drying methods. Drying in ambient conditions lead to a completely collapsed film with low porosity and high density. Better results were achieved by freeze-drying, which can in turn be subcategorized into three groups. In vacuum freeze-drying, the hydrogel is placed in a vacuum chamber, which is rapidly evacuated, leading to freezing of the water (see Figure 3.8b). Subsequent sublimation of the ice proceeded until a highly aggregated aerogel was achieved. Dipping the hydrogel into liquid nitrogen (−196 °C) prior to sublimation yielded smaller aggregates and more fibrillar aerogels. Even faster freezing by dipping into cooled liquid propane (−100 °C) yielded a completely fibrillar aerogel for thin samples, yet crystallization fronts and aggregation were observed in thicker samples. The difference in the freeze-drying methods was attributed to the *Leidenfrost* effect,[16] where a boiling liquid forms an insulating gas layer (see Figure 3.8d), which hinders heat transfer and thus allows larger crystals to form. In freeze-drying, the hydrogel acts as the "hot surface". Liquid nitrogen lies at its boiling point and thus all the cooling is due to enthalpy of boiling, which creates a large amount of insulating nitrogen gas. However, liquid propane can be cooled well below its boiling point (*ca.* −42 °C) by using liquid nitrogen. Therein heat transfer is solely due to the heat capacity of the liquid and boiling is suppressed, which prevents the insulating gas layer from forming. This more rapid freezing by liquid propane leads to formation of smaller ice crystals when compared to liquid nitrogen and thus the aggregation of fibrils is mostly inhibited. Employing supercritical CO_2-drying facilitated the creation of completely fibrillar aerogels, yet aggregation of the fibrils into "flocs" during the solvent-exchange process was evident, at least for ethanol and acetone, which were used as the intermediate solvents in the study. CO_2 is insufficiently soluble in water to allow exchange directly from the hydrogel, yet instead organogels in a compatible solvent needed to be prepared by solvent-exchange. Furthermore, the more fibrillar aerogels suffered from worse mechanical properties, and the "best" samples in terms of fibrillarity, were fragile to handle. However, the aggregated aerogels (vacuum freeze-drying and liquid

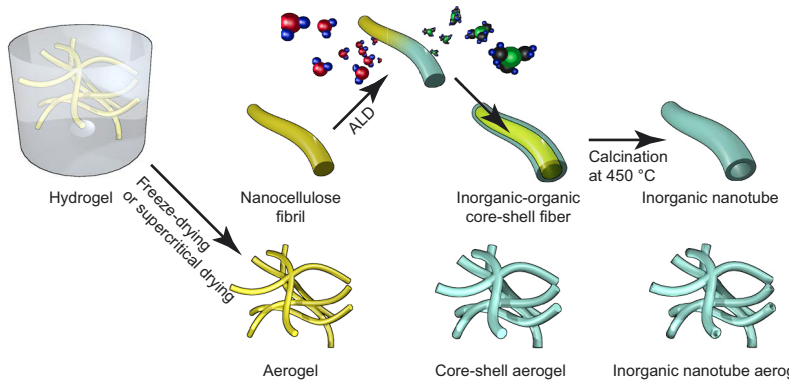

Figure 3.9. Schematic representation of the process of creating organic–inorganic hybrid core–shell aerogels as well as purely inorganic hollow-core nanotubes. Adapted with permission from Publication IV. Copyright ©2011 American Chemical Society.

nitrogen freeze-drying) exhibited ductile behavior. Therefore, it seems that the sheet-like aggregation strengthens the aerogels.

3.4 Functionalization of Nanocellulose Aerogels

The nanocellulose aerogels were functionalized with three inorganics: titanium dioxide (TiO_2), zinc oxide (ZnO), and aluminum oxide (Al_2O_3). These materials could be easily uniformly coated by ALD onto the aerogels to provide functionality. TiO_2 and ZnO are inorganic wide-bandgap semiconductors, which exhibit photo-switchable wetting.[129–131] Al_2O_3 on the other hand is a hydrophilic material, which creates extremely smooth amorphous coatings on various substrates and here it was used as a reference material.

The ALD deposition employed well-established routes for metalorganics (diethylzinc/water and trimethylaluminum/water processes) and halides (titanium tetrachloride/water process).[100] The procedure for creating coated nanocellulose aerogels is shown schematically in Figure 3.9. The aerogel substrates are both porous and sensitive to high temperature, which implied restrictions for the ALD procedure. The reactor temperature employed was kept at 150 °C to prevent thermal decomposition of the cellulose network and the pulse/purge times were increased to 20 s to allow precursor diffusion into the aerogel.

A typical procedure of 50 cycles of ALD resulted in hybrid organic–inorganic core–shell structures, which are depicted in Figure 3.10. The TiO_2-coated aerogels were repellent to water yet absorbing organic solvents, which lead to an application described in Section 4.3. Further calcination of the samples lead to completely inorganic hollow-core nanotubes, and possible crystallization of the inorganic layer. Crushing the inorganic aerogels with a mortar allowed the

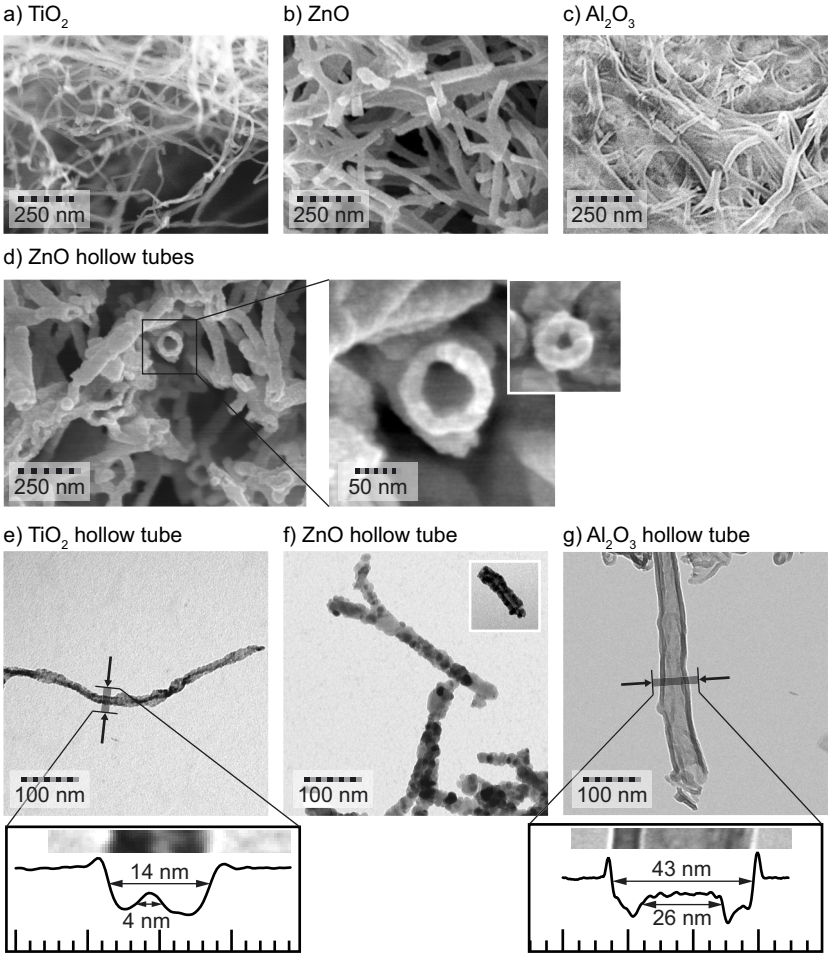

Figure 3.10. Nanocellulose aerogels functionalized with inorganic coatings by atomic layer deposition. a)–c) Scanning electron micrographs from TiO_2, ZnO, and Al_2O_3 -coated organic–inorganic core–shell aerogels. d) ZnO aerogel after calcination at 450 °C exhibits hollow nanotubes. e)–g) Transmission electron micrographs of the calcinated aerogels. TiO_2 and Al_2O_3 exhibit empty cores and shell thicknesses of *ca.* 5 nm and 8.5 nm. ZnO has crystallized, which renders the determination of the shell thickness from the micrograph impossible. The inset in f) shows a tube, where the core is barely visible. Adapted with permission from Publication IV. Copyright ©2011 American Chemical Society.

nanotubes to be dispersed into ethanol and then subsequentially cast as films onto conductive glass substrates. These nanotube films exhibited interesting atmospheric-responsive functionalities, which are described in Section 4.2.

3.5 Contact Angle Measurements

Contact angle measurements were performed on an *Attension Theta* (Biolin Scientific) optical tensiometer, which featured a computer-controlled microliter syringe, blue light source, and a high speed camera. The results were analyzed on a proprietary software from the manufacturer, which employed axisymmetric drop shape analysis based on solving the Young–Laplace equation. The sensitivity of the device at extremely high contact angles would need to be improved for it to yield reliable and reproducible results. However, a standard procedure for the measurements yielded self-consistent results, which can be compared to each other. It should be pointed out that in literature the reliability of contact angle measurements of superhydrophobic surfaces is usually not estimated and comparisons between studies should always be performed with caution.

The standard procedure employed for measuring advancing and receding contact angles followed these guidelines (see Figure 3.11). (1) Deposit a small (*ca.* 1 µl) drop of de-ionized, de-gassed water on the surface while leaving the needle inside the drop. (2) Increase the drop size until > 10 µl and continuously record the contact angle at different volumes. (3) Measure the advancing contact angle from the plateau region. (4) Increase drop volume to a value estimated by the theory in Section 2.6.1, which is typically around 50 µl. (5) Decrease drop volume until *ca.* 2 µl and continuously record the contact angle. (6) Read the receding contact angle from the plateau region. (7) If the plateau region was unreachable, try to increase the volume or decrease the volume displacement rate.

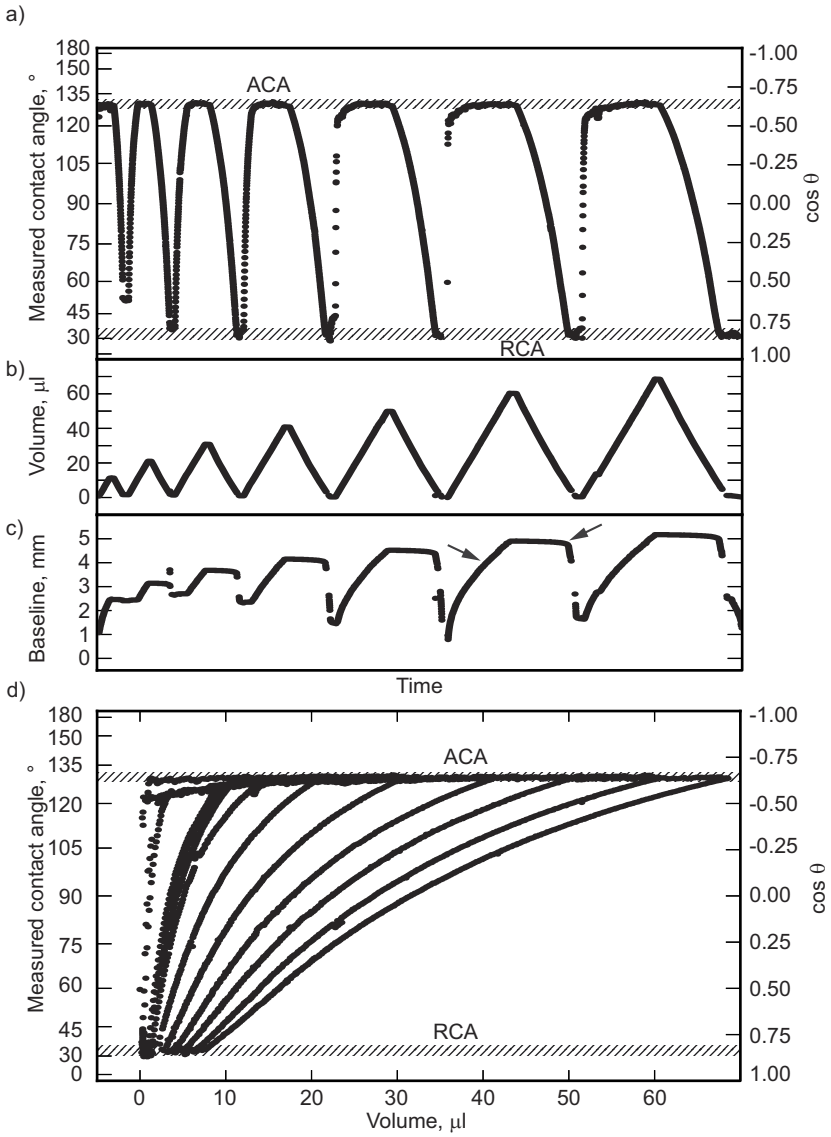

Figure 3.11. Example contact angle measurement of a surface with extremely high hysteresis. a) A contact angle vs. time plot displays seven measurement cycles each one ending up at a higher volume than the previous. b) Volume vs. time. c) Baseline length vs. time. Arrows display the advancing and receding regions of a certain cycle. d) Contact angle plotted against the drop volume depicts the behavior most clearly. Both advancing and receding contact angle plateaus are visible. Adapted with permission from Publication I. Copyright ©2013 American Chemical Society.

4. Applications

"Knowledge is of no value unless you put it into practice."
– Anton Pavlovich Chekhov

In addition to the theory and experimental results presented, this section introduces applications for the novel materials. All of the demonstrations exhibit a proof–of–concept nature while leaving up-scaling and manufacturing challenges to further studies. Three applications are presented as case-studies.

4.1 Displaying and Storing Optical Information in Plastron

Section 3.2 described the physical properties of hierarchically superhydrophobic micropost/silicone nanofilament surfaces. The bi-stability of the plastron under water allowed to write and store information on the surface using a jet of water (Figure 4.1). After immersion, the surface adopted the micro-Cassie wetting state, which is specularly reflective due to the flat water–air interface. A jet of water forced the water–air interface to protrude between the microposts, which created a highly curved surface, and the surface became diffusively reflective. Therefore the parts inscribed with the nano-Cassie state appear white in Figure 4.1 and the micro-Cassie state looks darker. A stability test, where a surface with both nano-Cassie and micro-Cassie regions was immersed in a container of water for *ca.* 30 days, revealed that both of the states were stable in that time period. Therefore, the surface warrants to be described as a bi-stable.

The diffuse scattering from the nano-Cassie regions was over 10 times higher than from the micro-Cassie regions. The contrast (*i.e.* ratio of the reflectivities of the states) is far behind commercial liquid-crystal displays or other bi-stable reflective technologies, yet clearly readable in suitable lighting conditions. A display using this technology might find a niche market inside the bi-stable reflective display technologies, if it would be developed further. Another application for this material is storing of information. Basically a piece of information (*i.e.* a "bit") could be stored in the area between four posts, creating a packing density equivalent to a compact disc of 11 megabytes (without any error correc-

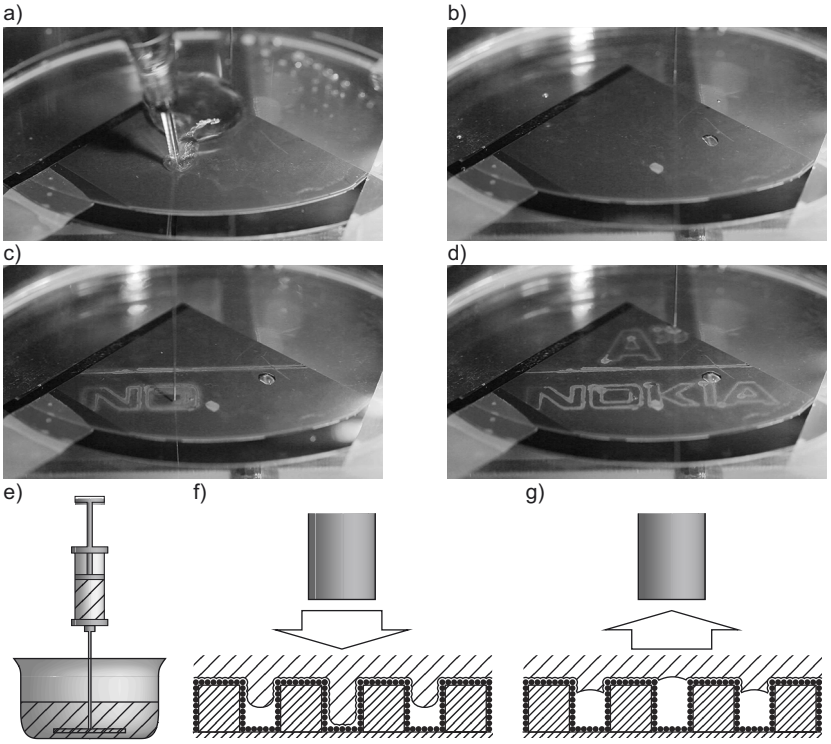

Figure 4.1. Photograph series of writing information on a hierarchically superhydrophobic surface. a) Surface is being immersed under water. b) Surface is fully under water. c) A jet of water "writes" onto the surface. d) Writing has completed. e) Schematic representation of the writing process. f) Water jet from the needle pushes the water–air interface downwards and causes a wetting transition. g) Reverse transition demonstrated: suction from needle "lifts" water–air interface to the top of the posts.

tion bits). However, the pitch of the posts is not limited to 10 µm, and already 1 µm pitch would lead to 1.1 GB per area of a compact disc. Again, this kind of water-based optical storage would require a specialist application. The benefits of the system include permanent erasability of the written data by simply taking the surface out from water. It is also immune to electrical and magnetic interference, since it is written by pressure and read by optical means.

4.2 Humidity Sensor with a Fast Response

Humidity has proved difficult to measure, especially in the low humidity range. The most traditional humidity sensors employ humidity-induced mechanical changes in materials, such as the length of a human hair or the curving of a metal–paper coil. Nowadays, the most accurate humidity sensors work on the dew-point principle, where water condensates onto a cooled mirror and the temperature is logged. There exists also capacitive and resistive humidity sensors which exhibit good accuracy and response times.[132] Lately, TiO_2 nanotube ar-

rays and nano-wires have been created for humidity sensing applications and they have shown promising results on a range of applications.[133,134] However, most of the sensors consisted of a planar surface with relatively short nanowires or nanotubes. To date, no TiO_2-based sensors created using percolating three-dimensional networks of nanotubes existed. The benefit of such a system is the high surface area compared to the volume of the sensor. This kind of system could possibly exhibit an enhanced response to external stimuli, such as humidity.

Publication IV demonstrates a humidity sensor based on a TiO_2-nanotube film on a conductive glass substrate, which is shown in Figure 4.2. Nanocellulose aerogels were ALD-coated with a uniform layer of TiO_2 followed by calcination, which effectively removed the organic core from the fibers. After calcination the samples were extremely brittle and they were thus mixed with a solvent and mechanically ground into a slurry. The slurry was blade-casted on a conductive surface, such as fluorine-tin oxide (FTO) glass, an example of which is shown in Figure 4.2a. Placing the substrate in a humidity chamber allowed to measure its electric response using a constant current source and a voltage meter. At constant current, the measured voltage was inversely proportional to the chamber humidity, as shown in Figure 4.2e. The response time was exceptionally fast, on the order of 1–10 s, which is comparable to state-of-the-art sensors.[135–137] For example, the Vaisala temperature/humidity logger employed (HMT333/Humicap 180) for the reference humidity measurements reported a response time of $t_{90\%} = 8$ s.[138] The resistance response was linearly decreasing when drawn on a semi-logarithmic scale as in Figure 4.2f. Due to the fast response time, an improved version of the TiO_2-nanotube film could prove interesting in a humidity sensor application.

4.3 Selective Oil-Absorbent

Collecting oil from the surface of water under marine environment is a challenging task, which is further hindered by the fact that oil tends to spread into a thin film on water and also to emulsify to create a substance that is extremely difficult to separate.[139] The extent of the difficulties realized at the Gulf of Mexico in 2010, when an explosion on an oil rig caused the death of 11 people and a spill of 4.9 million US barrels, which equals the size of an oil slick *ca.* 10×10 km^2 and 1 cm thick.[140] Furthermore, the amount of oil shipped on the Baltic Sea in 2012 equaled roughly 150 million metric tons per year and roughly 2000 oil spills (mostly small and land-based) occur each year in Fin-

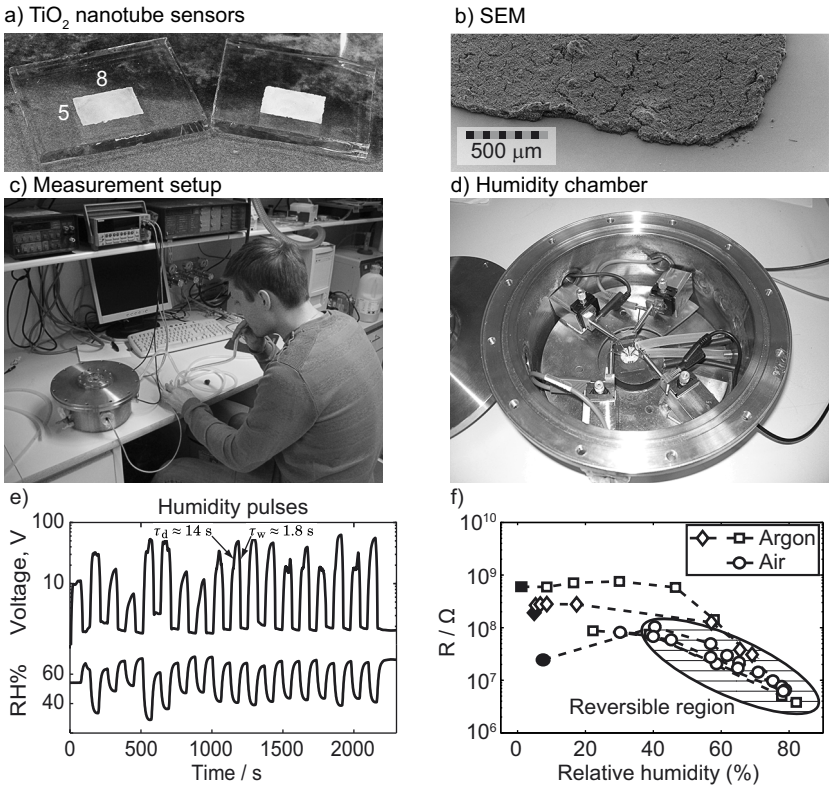

Figure 4.2. TiO_2-nanotube humidity sensor. a) Photograph of two sensor modules on conductive glass. b) Scanning electron micrograph of a nanotube-film. c) The measurement setup comprises a sourcemeter, some wiring, humidity chamber, and gas inlets. Exhaling through a pipe into the chamber provided the first rudimentary method of changing humidity of the sample. d) The sample lies at the center of the humidity chamber together with the current source and voltage probes. e) A pulsing humidity experiment and voltage response of the sample at constant current. f) Humidity vs. resistance plot exhibits a log-linear region around 40–80% relative humidity. Adapted with permission in part from Publication IV. Copyright ©2011 American Chemical Society.

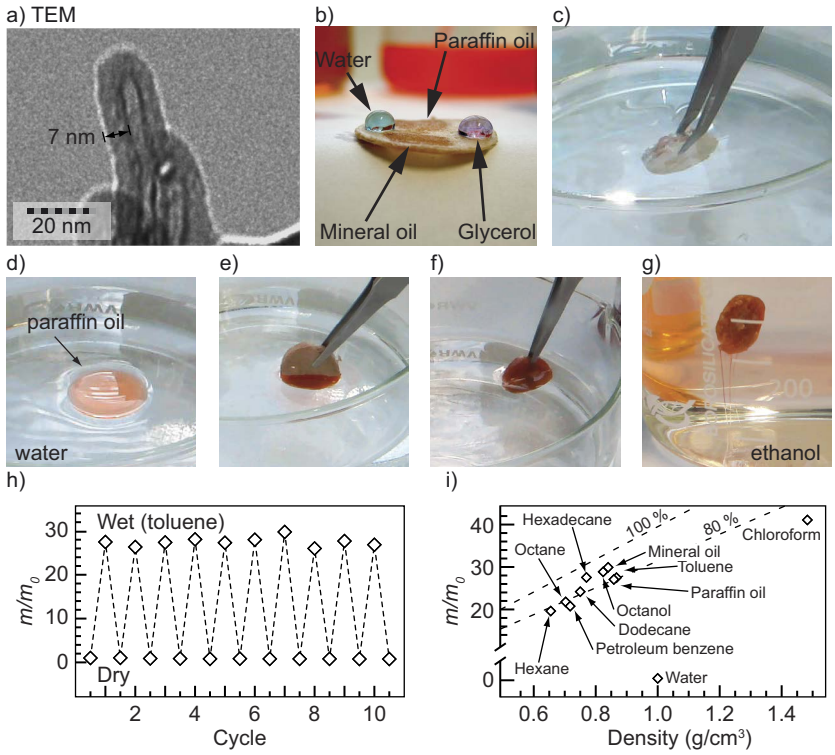

Figure 4.3. TiO_2-coated nanocellulose aerogel oil absorbents. a) Transmission electron micrograph of a coated cellulose nanofibril. b) Highly polar liquids, such as water and glycerol remained as drops on the aerogel, while oils were readily absorbed. c) Aerogel immersed in water did not wet, yet a layer of air remained on the surface. d) Paraffin oil slick floating on water. e)-f) Oil was absorbed using a aerogel pellet. g) Oil was released from the aerogel after immersion in ethanol or another solvent. h) Aerogel was cyclically soaked in toluene and subsequentially dried. i) Mass-based absorption capacity of the aerogel for a number of solvents and oils. Dashed lines represent the volume-based absorption capacity. Adapted with permission in part from Publication V. Copyright ©2011 American Chemical Society.

land.[141]

When oil has spread on the surface of water it is beneficial to absorb it into a solid material, which is more facile to collect. There are commercial polypropylene oil collection mats available, and their oil-intake ability can be as high as 15 times their own weight, yet up to 50% of the oil leeches out of the mat once its removed from the spill.[142,143] Researchers have created materials, such as silica aerogels[144–146] and carbon nanotube -based sponges,[147,148] which have shown oil absorption capacities up to 2–237 times their original dry weight. These impressive results, especially related to the aerogels, give reason to expect a similar behavior from the TiO_2-coated nanocellulose aerogels.

To realize a nanocellulose-based oil absorbent, Publication V employed ALD-coated freeze-dried aerogels with a thin uniform layer of TiO_2, which provided hydrophobicity for the material. The resulting aerogels exhibited hydrophobic, yet oleophilic properties, and while water drops remained as drops, oils were

readily absorbed, as shown in Figure 4.3. The aerogel could absorb an oil slick, roughly equal to its own volume, from the surface of water without absorbing any water. Furthermore, the oil could be released from the pellet by immersion under ethanol or another non-polar solvent. The aerogels could be reused several times without degradation, as shown by the toluene absorption test in Figure 4.3h. The absorption capacity, as determined by weight, ranged from *ca.* 20 to 40 times the original dry weight. The apparently large variation was due to the different densities of the absorbed liquids. Therefore, the study also determined the volume-based absorption capacity, which equaled *ca.* 80–90% for most liquids.

Another aspect to be considered, is the effect of liquid surface tension to the absorbed amount. A simplistic assumption of vertical capillaries, yields the well-known Jurin's law[8] for the height of capillary rise:

$$h = \frac{2\gamma\cos\theta}{\rho g r}, \tag{4.1}$$

where r is the diameter of the pore, and an aerogel absorbent floating on the surface is able to absorb liquid up to a height of h. If h is larger than the thickness of the aerogel, the whole pellet is soaked, otherwise the top part remains dry. For hexane, $\gamma/\rho \approx 28$ cm/s^2, r is roughly 1 µm, and θ can be approximated to be $< 45°$. These values yield $h \gtrsim 4$ m, which makes the thickness of the aerogel insignificant for the absorbed amount. The expected behavior for the absorbed amount would be $m \sim \gamma$, yet this kind of dependence was not observed, which is in contrast to results by Rao *et al.*[145], where a clear dependence between surface tension and absorbed mass was reported. Their scaling law presented was based on the mass that a *single capillary* could uphold. Modeling an aerogel as a single capillary quite obviously does not portray the situation well. However, the contradicting results could be mostly explained by the dependence of density and surface tension (because for simple liquids both are related to the cohesion energy) for the liquids used in the study.

Nanocellulose-based oil absorbents could prove useful as a countermeasure for oil spill cleanup under marine environment providing the cost to manufacture would decrease. Nanocellulose can already be produced at industrial scale, and freeze-drying and ALD have already found their way into production of various consumables. Furthermore, there exist even more feasible hydrophobicing methods, such as certain surfactants and waxes, that might facilitate the production. Therefore, a material created using these or similar processes could well be feasible in the future.

5. Conclusions and Outlook

"Surprising what you can dig out of books
if you read long enough, isn't it?"
– Robert Jordan

This thesis described basic concepts, material characterization, as well as applications, which are all related to wetting phenomena. The most important results are summarized below together with some insight into where the research might be directed in the future.

Publication I described a method to reliably measure the receding contact angle of a surface with hysteresis. The concept based on geometric arguments and a simple model for the measurement procedure. Therein, the contact line of a drop on a surface was assumed to be static until the receding (or advancing) contact angle was reached. The model produced results, which were verified by experiments. A Young–Laplace correction yielded more accurate results when large drops were employed. To this day, many publications have not reported the receding contact angle, yet this study demonstrated that the measurement should be possible for all surfaces, when sufficient care is taken. Furthermore, a novel definition for superhydrophobicity was proposed: "A superhydrophobic surface exhibits a *receding* contact angle larger than 150°."

Publication II introduced a kinetic growth model for the condensation synthesis of silicone nanofilaments. The novelty of the model was that it aims to explain in which way the break of symmetry occurs when the tetragonal constituent molecules start to arrange onto a surface. The model proposed that pressure pockets form inside a partially cross-linked film, which then subsequently bursts or expands to form the silicone nanofilaments. Experimental evidence, especially the hollow tubes sometimes observed, provided preliminary proof for the process. Furthermore, the creation of silicone *macro*filaments under water provided insight into the processes, even though the situation was not exactly similar. Further studies should be able to test the model hypothesis, as it provides some predictions that can be tested. For example, the growth should be different at curved surfaces, and also on chemically heterogeneous surfaces.

Publication III introduced a theoretical analysis, which showed that there are

benefits in creating hierarchically wetting surfaces. The hierarchy extended the geometries, which exhibited a stable non-wetting state, and also enabled reverse transitions and bi-stable operation. The theory was tested by creating a hierarchically superhydrophobic surface by employing lithographic methods and a silicone nanofilament coating. The surface was immersed under water and a stream of water was able to "write" on the surface. The writing consisted of a wetting transition into the more-wetting state. The writing could be erased simply by reversing the direction of the jet, *i.e.* sucking water from right above the surface. Both states were stable for a long period of time under water. In the future, the system might find applications in bi-stable display technology or optical data storage.

Publications IV and V demonstrated functionalized nanocellulose aerogels. The drying method of the nanocellulose hydrogel proved to be an important factor to the morphology of the resulting aerogel. Drying under ambient conditions lead to a complete collapse of the structure, while freeze-drying and supercritical drying methods yielded aerogels. The speed of the freezing determined the amount of sheet-like aggregates observed instead of fibers, and also the pore size of the largest features. Slow freezing, as in vacuum freeze-drying, resulted in large pores, heavy aggregation and ductile behavior, while the fastest freezing in liquid propane yielded almost fully fibrillar aerogels with minimal aggregation. Supercritical CO_2-drying appeared to retain the original structure of the hydrogel, yet the solvent exchange process from water to ethanol or acetone, might have led to flocculation.

Publication IV demonstrated a resistive/capacitive humidity sensor with fast response based on TiO_2-coated nanocellulose aerogels. The ALD-coated nanofibrils were crushed and dispersed into ethanol before casting them as films on conductive substrates. Simply measuring the voltage across the films, while providing constant current, yielded fast response to atmospheric humidity. Furthermore, a linear reproducible response to humidity was observed at humidity range 40–80%. The mechanism was attributed to the high contact area of the nanotubes, which might have amplified the response. Perhaps this kind of detector might be competitive with other types of sensors, provided that the cost to manufacture would be low.

A TiO_2-coated aerogel exhibiting hydrophobic yet oleophilic behavior was introduced in Publication V. The aerogel was able to absorb almost its own volume of oils from the surface of water without absorbing any water. The oil from the pellets could be removed by simple immersion in an organic solvent, or the whole pellet could be burned in a furnace. The aerogels could be re-used sev-

eral times without loss of absorption capacity. These proof-of-concept absorbent pellets might prove useful, yet collaboration with the people working actually with the oil spills would have to be started to assess the true feasibility.

This work only scraped the very surface of the topic of wetting. There are endless possibilities for further research — both theoretical and practical. One important question is what is the time-scale of the wetting transitions observed in Publication III. There could be both theoretical and experimental approaches to this problem. In fact, there are already preliminary results from an experiment where the air layer on a hierarchically superhydrophobic surface is manipulated by using a periodic pressure profile. This experiment should, in the end, provide information about the dynamics of the transitions, which need to be understood also from a theoretical point-of-view. The nanocellulose aerogels have been extensively studied, yet they provide constantly new insights. For example, the wetting behavior of purely fibrillar hydrophobic aerogels appears to be different from those with sheet-like aggregates. From a material view point, the cellulose nanofibrils appear highly similar to the silicone nanofilaments, which raises the question could hydrophobized nanofibrils act similar to the nanofilaments. Whether the research continues to explore the basic concepts of wetting, interesting novel materials, or applications of these, there will be many interesting phenomena still to conquer in the future.

Notes and References

[1] R. D. DEEGAN, O. BAKAJIN, and T. F. DUPONT. Capillary Flow as the Cause of Ring Stains from Dried Liquid Drops. *Nature* **1997**, *389*, 827–829.

[2] H. B. ERAL, D. J. C. M. 'T MANNETJE, and J. M. OH. Contact Angle Hysteresis: A Review of Fundamentals and Applications. *Colloid and Polymer Science* **2012**, *291*, 247–260.

[3] B. M. WEON and J. H. JE. Fingering Inside the Coffee Ring. *Physical Review E* **2013**, *87*, 013 003.

[4] C. G. L. FURMIDGE. Studies at Phase Interfaces. I. The Sliding of Liquid Drops on Solid Surfaces and a Theory for Spary Retention. *Journal of Colloid Science* **1962**, *17*, 309–324.

[5] P. S. DE LAPLACE. *Oeuvres Complètes de Laplace, t IV, Supplemént au Livre X du Traité de la Mécanique Céleste* and *2ème Supplément au Livre X*, (Gauthier–Villars, 1804). Referenced in Ref. 8.

[6] Y. PERELMAN. *Physics for Entertainment* (Hyperion, 1936).

[7] H. BIANCO and A. MARMUR. Gibbs Elasticity of a Soap Bubble. *Journal of Colloid and Interface Science* **1993**, *158*, 295–302.

[8] P.-G. DE GENNES, F. BROCHARD-WYART, and D. QUÉRÉ. *Capillarity and Wetting Phenomena: Drops, Bubbles, Pearls, Waves* (Springer Science+Business Media, Inc., 2004).

[9] Also, J. PLATEAU. *Statique Expérimentale et Théoritique des Liquids Soumis aux Seules Forces Moléculaires* (Gauthiers–Villars, 1873), which I was not able to find a copy, yet is referenced in Refs. 8,10,11.

[10] LORD RAYLEIGH. On the Instability of Jets. *Proceedings of the London Mathematical Society* **1878**, *10*, 4–13.

[11] X. D. SHI, M. P. BRENNER, and S. R. NAGEL. A Cascade of Structure in a Drop Falling from a Faucet. *Science* **1994**, *265*, 219–222.

[12] The following passage allegedly refers to "tears of wine": *See not wine when it showeth itself red, When it giveth in the cup its colour, It goeth up and down through the upright*. R. YOUNG. *Young's Literal Translation of the Bible* (1898), Proverbs 23:31.

[13] J. B. FOURNIER and A. M. CAZABAT. Tears of Wine. *Europhysics Letters* **1992**, *20*, 517–522.

[14] R. VUILLEUMIER, V. EGO, L. NELTNER, and A. M. CAZABAT. Tears of Wine: The Stationary State. *Langmuir* **1995**, *11*, 4117–4121.

[15] R. W. GORE. *Process for Producing Porous Products*, U.S. Patent 3,953,566 (April 1976).

[16] An English transcript of the original article from 1756, which was written in Latin, *De Aquae Communis Nonnullis Qualitatibus Tractatus*, is found at J. G. LEIDENFROST *International Journal of Heat and Mass Transfer* **1966**, *9*, 1153–1166.

[17] I. U. VAKARELSKI, N. A. PATANKAR, J. O. MARSTON, D. Y. C. CHAN, and S. T. THORODDSEN. Stabilization of Leidenfrost Vapour Layer by Textured Superhydrophobic Surfaces. *Nature* **2012**, *489*, 274–277.

[18] Credits for the photographs go to Roger McLassus (the faucet), Brocken Inaglory (rain drop on a window), Shaddack (Gore-Tex® micrograph), Wart Dark (Gore-Tex® schematic), FlagSteward ("tears of wine"), Michael Gasperl (lotus leaf), and William Thielicke (self-cleaning schematic).

[19] W. BARTHLOTT and C. NEINHUIS. Purity of the Sacred Lotus, or Escape from Contamination in Biological Surfaces. *Planta* **1997**, *202*, 1–8.

[20] Referenced in Ref. 19, yet it is written in German: A. LUNDSTRÖM. *Pflanzenbiologische Studien*. Uppsala University, 1884.

[21] R. R. DAVIES. Wettability and the Capture, Carriage and Deposition of Particles by Raindrops. *Nature* **1961**, *191*, 616–617.

[22] Z. GUO, W. LIU, and B.-L. SU. Superhydrophobic Surfaces: From Natural to Biomimetic to Functional. *Journal of Colloid and Interface Science* **2011**, *353*, 335–355.

[23] L. GAO and T. J. MCCARTHY. How Wenzel and Cassie Were Wrong. *Langmuir* **2007**, *23*, 3762–3765.

[24] S. WANG and L. JIANG. Definition of Superhydrophobic States. *Advanced Materials* **2007**, *19*, 3423–3424.

[25] L. GAO and T. J. MCCARTHY. Teflon Is Hydrophilic. Comments on Definition of Hydrophobic, Shear versus Tensile Hydrophobicity, and Wettability Characterization. *Langmuir* **2008**, *24*, 546–550.

[26] A. MARMUR. A Guide to the Equilibrium Contact Angles Maze. In K. L. MITTAL, editor, "Contact Angle, Wettability and Adhesion, Volume 6", chap. 1.1 (VSP, Leiden, 2009).

[27] A. MARMUR and E. BITTOUN. When Wenzel and Cassie Are Right: Reconciling Local and Global Considerations. *Langmuir* **2009**, *25*, 1277–1281.

[28] G. MCHALE. All Solids, including Teflon, Are Hydrophilic (to Some Extent), but Some Have Roughness Induced Hydrophobic Tendencies. *Langmuir* **2009**, *25*, 7185–7187.

[29] M. STROBEL and C. S. LYONS. An Essay on Contact Angle Measurements. *Plasma Processes and Polymers* **2011**, *8*, 8–13.

[30] A. J. B. MILNE and A. AMIRFAZLI. The Cassie Equation: How It Is Meant to Be Used. *Advances in Colloid and Interface Science* **2012**, *170*, 48–55.

[31] C. W. EXTRAND and S. I. MOON. Which Controls Wetting? Contact Line Versus Interfacial Area: Simple Experiments on Capillary Rise. *Langmuir* **2012**, *28*, 15 629–15 633.

[32] A. MARMUR. Hydro- Hygro- Oleo- Omni-Phobic? Terminology of Wettability Classification. *Soft Matter* **2012**, *8*, 6867–6870.

[33] T. YOUNG. An Essay on the Cohesion of Fluids. *Philosophical Transactions of the Royal Society of London* **1805**, *95*, 65–87.

[34] R. E. JOHNSON. Conflicts Between Gibbsian Thermodynamics and Recent Treatments of Interfacial Energies in Solid-Liquid-Vapor Systems. *Journal of Physical Chemistry* **1959**, *63*, 1655–1658.

[35] P. ROURA and J. FORT. Local Thermodynamic Derivation of Young's Equation. *Journal of Colloid and Interface Science* **2004**, *272*, 420–429.

[36] R. N. WENZEL. Resistance of Solid Surfaces to Wetting by Water. *Industrial Engineering Chemistry* **1936**, *28*, 988–994.

[37] R. N. WENZEL. Surface Roughness and Contact Angle. *Journal of Physical and Colloid Chemistry* **1949**, *53*, 1466–1567.

[38] T. NISHINO, M. MEGURO, K. NAKAMAE, M. MATSUSHITA, and Y. UEDA. The Lowest Surface Free Energy Based on $-CF_3$ Alignment. *Langmuir* **1999**, *15*, 4321–4323.

[39] A. B. D. CASSIE and S. BAXTER. Wettability of Porous Surfaces. *Transactions of the Faraday Society* **1944**, *40*, 546–551.

[40] A. MARMUR. From Hygrophilic to Superhygrophobic: Theoretical Conditions for Making High-Contact-Angle Surfaces from Low-Contact-Angle Materials. *Langmuir* **2008**, *24*, 7573–7579.

[41] N. A. PATANKAR. On the Modeling of Hydrophobic Contact Angles on Rough Surfaces. *Langmuir* **2003**, *19*, 1249–1253.

[42] A. LAFUMA and D. QUÉRÉ. Superhydrophobic States. *Nature Materials* **2003**, *2*, 457–460.

[43] J. BICO, C. MARZOLIN, and D. QUÉRÉ. Pearl Drops. *Europhysics Letters* **1999**, *47*, 220–226.

[44] Z. YOSHIMITSU, A. NAKAJIMA, T. WATANABE, and K. HASHIMOTO. Effects of Surface Structure on the Hydrophobicity and Sliding Behavior of Water Droplets. *Langmuir* **2002**, *18*, 5818–5822.

[45] B. HE, N. A. PATANKAR, and J. LEE. Multiple Equilibrium Droplet Shapes and Design Criterion for Rough Hydrophobic Surfaces. *Langmuir* **2003**, *19*, 4999–5003.

[46] D. BARTOLO, F. BOUAMRIRENE, E. VERNEUIL, A. BUGUIN, P. SILBERZAN, and S. MOULINET. Bouncing or Sticky Droplets: Impalement Transitions on Superhydrophobic Micropatterned Surfaces. *Europhysics Letters* **2006**, *74*, 299–305.

[47] B. HIPP, I. KUNERT, and M. DÜRR. Systematic Control of Hydrophobic and Superhydrophobic Properties Using Double-Rough Structures Based on Mixtures of Metal Oxide Nanoparticles. *Langmuir* **2010**, *26*, 6557–6560.

[48] C. DELLA VOLPE, D. MANIGLIO, M. MORRA, and S. SIBONI. The Determination of a "Stable-Equilibrium" Contact Angle on Heterogeneous and Rough Surfaces. *Colloids and Surfaces A: Physicochemical and Engineering Aspects* **2002**, *206*, 47–67.

[49] E. L. DECKER and S. GAROFF. Using Vibrational Noise to Probe Energy Barriers Producing Contact Angle Hysteresis. *Langmuir* **2006**, *12*, 2100–2110.

[50] M. A. RODRÍGUEZ-VALVERDE, F. J. MONTES RUIZ-CABELLO, and M. A. CABRERIZO-VÍLCHEZ. A New Method for Evaluating the Most-Stable Contact Angle Using Mechanical Vibration. *Soft Matter* **2011**, *7*, 53–56.

[51] F. J. MONTES RUIZ-CABELLO, M. A. RODRÍGUEZ-VALVERDE, and M. CABRERIZO-VÍLCHEZ. A New Method for Evaluating the Most Stable Contact Angle Using Tilting Plate Experiments. *Soft Matter* **2011**, *7*, 10 457–10 461.

[52] T.-S. JIANG, O. H. SOO-GUN, and J. C. SLATTERY. Correlation for Dynamic Contact Angle. *Journal of Colloid and Interface Science* **1979**, *69*, 74–77.

[53] J. E. SEEBERGH and J. C. BERG. Dynamic Wetting in the Low Capillary Number Regime. *Chemical Engineering Science* **1992**, *47*, 4455–4464.

[54] M. BRACKE, F. VOEGHT, and P. JOOS. The Kinetics of Wetting: The Dynamic Contact Angle. In P. BOTHOREL and E. J. DUFOURC, editors, "Trends in Colloid and Interface Science III", vol. 79 of *Progress in Colloid & Polymer Science*, pp. 142–149 (Steinkopff, 1989).

[55] T. D. BLAKE and Y. D. SHIKHMURZAEV. Dynamic Wetting by Liquids of Different Viscosity. *Journal of Colloid and Interface Science* **2002**, *253*, 196–202.

[56] J. BILLINGHAM. Nonlinear Sloshing in Zero Gravity. *Journal of Fluid Mechanics* **2002**, *464*, 365–391.

[57] T. D. BLAKE. The Physics of Moving Wetting Lines. *Journal of Colloid and Interface Science* **2006**, *299*, 1–13.

[58] J. EGGERS and R. EVANS. Comment on "Dynamic Wetting by Liquids of Different Viscosity," by T. D. Blake and Y. D. Shikhmurzaev. *Journal of Colloid and Interface Science* **2004**, *280*, 537–8; discussion 539–41.

[59] C. ANDRIEU, C. SYKES, and F. BROCHARD. Average Spreading Parameter on Heterogeneous Surfaces. *Langmuir* **1994**, *10*, 2077–2080.

[60] The reference for this article is H. L. ROSANO. *Mém. Services Chim. État.* **1951**, *36*, 437, yet it proved challenging to locate this French journal. The equation was referred to in Ref. 4.

[61] G. MACDOUGALL and C. OCKRENT. Surface Energy Relations in Liquid/Solid Systems. I. The Adhesion of Liquids to Solids and a New Method of Determining the Surface Tension of Liquids. *Proceedings of the Royal Society A: Mathematical, Physical and Engineering Sciences* **1942**, *180*, 151–173.

[62] J. DRELICH, E. CHIBOWSKI, D. D. MENG, and K. TERPILOWSKI. Hydrophilic and Superhydrophilic Surfaces and Materials. *Soft Matter* **2011**, *7*, 9804–9828.

[63] T. ONDA, S. SHIBUICHI, N. SATOH, and K. TSUJII. Super-Water-Repellent Fractal Surfaces. *Langmuir* **1996**, *12*, 2125–2127.

[64] S. SHIBUICHI, T. YAMAMOTO, T. ONDA, and K. TSUJII. Super Water- and Oil-Repellent Surfaces Resulting from Fractal Structure. *Journal of Colloid and Interface Science* **1998**, *208*, 287–294.

[65] F. G. REICK. *Substrate Coated with Super-Hydrophobic Layers*, U.S. Patent 3,931,428 (Jan 1976).

[66] F. G. REICK. *Toys and Games Using Super-Hydrophobic Surfaces*, U.S. Patent 4,199,142 (April 1980).

[67] C. J. VAN OSS. *Interfacial Forces in Aqueous Media* (Marcel Dekker, Inc., New York, 1994).

[68] E. A. VOGLER. Structure and Reactivity of Water at Biomaterial Surfaces. *Advances in Colloid and Interface Science* **1998**, *74*, 69–117.

[69] Y. TIAN and L. JIANG. Wetting: Intrinsically Robust Hydrophobicity. *Nature Materials* **2013**, *12*, 291–292.

[70] C. GUO, S. WANG, H. LIU, L. FENG, and Y. SONG. Alteration of Polymer Surfaces Produced by Scraping. *Journal of Adhesion Science and Wettability* **2008**, *22*, 395–402.

[71] N. J. SHIRTCLIFFE, G. MCHALE, S. ATHERTON, and M. I. NEWTON. An Introduction to Superhydrophobicity. *Advances in Colloid and Interface Science* **2010**, *161*, 124–138.

[72] C. NEINHUIS and W. BARTHLOTT. Characterization and Distribution of Water-Repellent, Self-Cleaning Plant Surfaces. *Annals of Botany* **1997**, *79*, 667–677.

[73] M. MA and R. M. HILL. Superhydrophobic Surfaces. *Current Opinion in Colloid & Interface Science* **2006**, *11*, 193–202.

[74] D. QUÉRÉ. Wetting and Roughness. *Annual Review of Materials Research* **2008**, *38*, 71–99.

[75] B. KRASOVITSKI and A. MARMUR. Drops Down the Hill: Theoretical Study of Limiting Contact Angles and the Hysteresis Range on a Tilted Plate. *Langmuir* **2005**, *21*, 3881–3885.

[76] M. HOORFAR and A. W. NEUMANN. Axisymmetric Drop Shape Analysis (ADSA). In A. W. NEUMANN, R. DAVID, and Y. ZUO, editors, "Applied Surface Thermodynamics", chap. 3, pp. 107–174 (CRC Press, Boca Raton, 2010), 2nd ed.

[77] J.-H. ZIMMERMANN. *Silicone Nanofilaments as Functional Coatings: Properties, Applications and Modifications*. PhD Thesis, University of Zürich **2008**.

[78] G. R. J. ARTUS, S. JUNG, J. ZIMMERMANN, H.-P. GAUTSCHI, K. MARQUARDT, and S. SEEGER. Silicone Nanofilaments and Their Application as Superhydrophobic Coatings. *Advanced Materials* **2006**, *18*, 2758–2762.

[79] L. GAO and T. J. MCCARTHY. A Perfectly Hydrophobic Surface (θ_A/θ_R = 180°/180°). *Journal of the American Chemical Society* **2006**, *128*, 9052–9053.

[80] D.-A. E. ROLLINGS, S. TSOI, J. C. SIT, and J. G. C. VEINOT. Formation and Aqueous Surface Wettability of Polysiloxane Nanofibers Prepared via Surface Initiated, Vapor-Phase Polymerization of Organotrichlorosilanes. *Langmuir* **2007**, *23*, 5275–5278.

[81] J. ZIMMERMANN, G. R. J. ARTUS, and S. SEEGER. Long Term Studies on the Chemical Stability of a Superhydrophobic Silicone Nanofilament Coating. *Applied Surface Science* **2007**, *253*, 5972–5979.

[82] J. ZIMMERMANN, F. A. REIFLER, U. SCHRADE, G. R. J. ARTUS, and S. SEEGER. Long Term Environmental Durability of a Superhydrophobic Silicone Nanofilament Coating. *Colloids and Surfaces A: Physicochemical and Engineering Aspects* **2007**, *302*, 234–240.

[83] G. R. J. ARTUS, J. ZIMMERMANN, F. A. REIFLER, S. A. BREWER, and S. SEEGER. A Superoleophobic Textile Repellent Towards Impacting Drops of Alkanes. *Applied Surface Science* **2012**, *258*, 3835–3840.

[84] R. CHEN, X. ZHANG, Z. SU, R. GONG, X. GE, H. ZHANG, and C. WANG. Perfectly Hydrophobic Silicone Nanofiber Coatings: Preparation from Methyltrialkoxysilanes and Use as Water-Collecting Substrate. *The Journal of Physical Chemistry C* **2009**, *113*, 8350–8356.

[85] J. ZIMMERMANN, G. R. J. ARTUS, and S. SEEGER. Superhydrophobic Silicone Nanofilament Coatings. *Journal of Adhesion Science and Technology* **2008**, *22*, 251–263.

[86] H. S. KHOO and F.-G. TSENG. Engineering the 3D Architecture and Hydrophobicity of Methyltrichlorosilane Nanostructures. *Nanotechnology* **2008**, *19*, 345 603.

[87] L. GAO and T. J. MCCARTHY. $(CH_3)_3SiCl/SiCl_4$ Azeotrope Grows Superhydrophobic Nanofilaments. *Langmuir* **2008**, *24*, 362–364.

[88] M. JIN, J. WANG, Y. HAO, M. LIAO, and Y. ZHAO. Tunable Geometry and Wettability of Organosilane Nanostructured Surfaces by Water Content. *Polymer Chemistry* **2011**, *2*, 1658–1660.

[89] M. JIN, S. LI, J. WANG, M. LIAO, and Y. ZHAO. Controllable Fabrication of Organosilane Nano-Architectured Surfaces with Tunable Wettability. *Applied Surface Science* **2012**, *258*, 7552–7555.

[90] G. R. J. ARTUS and S. SEEGER. Scale-Up of a Reaction Chamber for Superhydrophobic Coatings Based on Silicone Nanofilaments. *Industrial & Engineering Chemistry Research* **2012**, *51*, 2631–2636.

[91] M. CALLIES and D. QUÉRÉ. On Water Repellency. *Soft Matter* **2005**, *1*, 55–61.

[92] D.-A. E. ROLLINGS and J. G. C. VEINOT. Polysiloxane Nanofibers via Surface Initiated Polymerization of Vapor Phase Reagents: A Mechanism of Formation and Variable Wettability of Fiber-Bearing Substrates. *Langmuir* **2008**, *24*, 13 653–13 662.

[93] C. DORRER and J. RÜHE. Condensation and Wetting Transitions on Microstructured Uultra-Hydrophobic Surfaces. *Langmuir* **2007**, *5*, 3820–3824.

[94] T. N. KRUPENKIN, J. A. TAYLOR, E. N. WANG, P. KOLODNER, M. HODES, and T. R. SALAMON. Reversible Wetting-Dewetting Transitions on Electrically Tunable Superhydrophobic Nanostructured Surfaces. *Langmuir* **2007**, *23*, 9128–9133.

[95] J. BOREYKO and C.-H. CHEN. Restoring Superhydrophobicity of Lotus Leaves with Vibration-Induced Dewetting. *Physical Review Letters* **2009**, *103*, 174 502.

[96] C. LEE and C.-J. KIM. Underwater Restoration and Retention of Gases on Superhydrophobic Surfaces for Drag Reduction. *Physical Review Letters* **2011**, *106*, 014 502.

[97] N. KUMARI and S. V. GARIMELLA. Electrowetting-Induced Dewetting Transitions on Superhydrophobic Surfaces. *Langmuir* **2011**, *27*, 10 342–10 346.

[98] G. MANUKYAN, J. M. OH, D. VAN DEN ENDE, R. G. H. LAMMERTINK, and F. MUGELE. Electrical Switching of Wetting States on Superhydrophobic Surfaces: A Route Towards Reversible Cassie-to-Wenzel Transitions. *Physical Review Letters* **2011**, *106*, 014 501.

[99] P. FORSBERG, F. NIKOLAJEFF, and M. KARLSSON. Cassie–Wenzel and Wenzel–Cassie Transitions on Immersed Superhydrophobic Surfaces Under Hydrostatic Pressure. *Soft Matter* **2011**, *7*, 104–109.

[100] R. L. PUURUNEN. Surface Chemistry of Atomic Layer Deposition: A Case Study for the Trimethylaluminum/Water Process. *Journal of Applied Physics* **2005**, *97*, 121 301.

[101] S. M. GEORGE. Atomic Layer Deposition: An Overview. *Chemical Reviews* **2010**, *110*, 111–131.

[102] T. SUNTOLA and J. ANTSON. *Method for Producing Compound Thin Films*.

[103] T. SUNTOLA. Atomic Layer Epitaxy. *Materials Science Reports* **1989**, *4*, 261–312.

[104] The reference A. M. SHEVYAKOV, G. N. KUZNETSOVA, V. B. ALESKOVSKII. *Chemistry of High-Temperature Materials* in *Proceedings of the Second USSR Conference on High-Temperature Chemistry of Oxides* **1965**, 149–155, was written in Russian, which is incomprehensible to the author. Referenced in Refs. 100,105.

[105] J. MALM. *Surface Functionalization by Atomic Layer Deposited Binary Oxide Thin Films*. Doctoral Dissertation, Aalto University School of Chemical Technology **2013**.

[106] J. A. KITTL, K. OPSOMER, M. POPOVICI, N. MENOU, B. KACZER, X. P. WANG, C. ADELMANN, M. PAWLAK, K. TOMIDA, A. ROTHSCHILD, B. GOVOREANU, R. DEGRAEVE, M. SCHAEKERS, M. ZAHID, A. DELABIE, J. MEERSSCHAUT, W. POLSPOEL, S. CLIMA, G. POURTOIS, W. KNAEPEN, C. DETAVERNIER, V. V. AFANAS'EV, T. BLOMBERG, D. PIERREUX, J. SWERTS, P. FISCHER, J. W. MAES, D. MANGER, W. VANDERVORST, T. CONARD, A. FRANQUET, P. FAVIA, H. BENDER, B. BRIJS, S. VAN ELSHOCHT, M. JURCZAK, J. VAN HOUDT, and D. J. WOUTERS. High-k Dielectrics for Future Generation memory devices. *Microelectronic Engineering* **2009**, *86*, 1789–1795.

[107] J. NIINISTÖ, K. KUKLI, M. HEIKKILÄ, M. RITALA, and M. LESKELÄ. Atomic Layer Deposition of High-*k* Oxides of the Group 4 Metals for Memory Applications. *Advanced Engineering Materials* **2009**, *11*, 223–234.

[108] BENEQ.COM. *Invisible Protection Against Tarnishing - Protective Coatings for Silver Application*. http://www.beneq.com/nsilver-anti-tarnish-coating.html (accessed 23.4.2013)

[109] D. J. COSGROVE. Growth of the Plant Cell Wall. *Nature Reviews Molecular Cell Biology* **2005**, *6*, 850–861.

[110] F. W. HERRICK, R. L. CASEBIER, K. J. HAMILTON, and K. R. SANDBERG. Microfibrillated Cellulose: Morphology and Accessibility. *Journal of Applied Polymer Science: Applied Polymer Symposium* **1983**, *37*, 797–813.

[111] A. F. TURBAK, F. W. SNYDER, and K. R. SANDBERG. Microfibrillated Cellulose, a New Cellulose Product: Properties, Uses, and Commercial Potential. *Journal of Applied Polymer Science: Applied Polymer Symposium* **1983**, *37*, 815–827.

[112] T. TANIGUCHI and K. OKAMURA. New Films Produced from Microfibrillated Natural Fibres. *Polymer International* **1998**, *47*, 291–294.

[113] M. PÄÄKKÖ, M. ANKERFORS, H. KOSONEN, A. NYKÄNEN, S. AHOLA, M. OSTERBERG, J. RUOKOLAINEN, J. LAINE, P. T. LARSSON, O. IKKALA, and T. LINDSTRÖM. Enzymatic Hydrolysis Combined with Mechanical Shearing and High-Pressure Homogenization for Nanoscale Cellulose Fibrils and Strong Gels. *Biomacromolecules* **2007**, *8*, 1934–1941.

[114] S. J. EICHHORN, A. DUFRESNE, M. ARANGUREN, N. E. MARCOVICH, J. R. CAPADONA, S. J. ROWAN, C. WEDER, W. THIELEMANS, M. ROMAN, S. RENNECKAR, W. GINDL, S. VEIGEL, J. KECKES, H. YANO, K. ABE, M. NOGI, A. N. NAKAGAITO, A. MANGALAM, J. SIMONSEN, A. S. BENIGHT, A. BISMARCK, L. A. BERGLUND, and T. PEIJS. Review: Current International Research into Cellulose Nanofibres and Nanocomposites. *Journal of Materials Science* **2009**, *45*, 1–33.

[115] A. ISOGAI, T. SAITO, and H. FUKUZUMI. TEMPO-Oxidized Cellulose Nanofibers. *Nanoscale* **2011**, *3*, 71–85.

[116] M. ANKERFORS. *Microfibrillated Cellulose: Energy-Efficient Preparation Techniques and Key Properties*. Licentiate's Thesis, KTH Royal Institute of Technology **2012**.

[117] S. S. KISTLER. Coherent Expanded Aerogels and Jellies. *Nature* **1931**, *127*, 741.

[118] N. HÜSING and U. SCHUBERT. Aerogels—Airy Materials: Chemistry, Structure, and Properties. *Angewandte Chemie International Edition* **1998**, *37*, 22–45.

[119] AEROGEL.ORG. *The History of Aerogel*. http://www.aerogel.org/?cat=38 (accessed 24.4.2013)

[120] AEROGEL.COM. *Aspen Aerogels: Insulation Products*. http://www.aerogel.com/products/overview-product.html (accessed 24.4.2013)

[121] SHIVERSHIELD.COM. *Shiver Shield: Warm Clothing for Cold Weather*. `http://www.shivershield.com` (accessed 24.4.2013)

[122] A. C. PIERRE and G. M. PAJONK. Chemistry of Aerogels and Their Applications. *Chemical Reviews* **2002**, *102*, 4243–4265.

[123] M. PÄÄKKÖ, J. VAPAAVUORI, R. SILVENNOINEN, H. KOSONEN, M. ANKERFORS, T. LINDSTRÖM, L. A. BERGLUND, and O. IKKALA. Long and Entangled Native Cellulose I Nanofibers Allow Flexible Aerogels and Hierarchically Porous Templates for Functionalities. *Soft Matter* **2008**, *4*, 2492–2499.

[124] H. JIN, Y. NISHIYAMA, M. WADA, and S. KUGA. Nanofibrillar Cellulose Aerogels. *Colloids and Surfaces A: Physicochemical and Engineering Aspects* **2004**, *240*, 63–67.

[125] R. GAVILLON and T. BUDTOVA. Aerocellulose: New Highly Porous Cellulose Prepared from Cellulose-NaOH Aqueous Solutions. *Biomacromolecules* **2008**, *9*, 269–277.

[126] R. T. OLSSON, M. A. S. AZIZI SAMIR, G. SALAZAR-ALVAREZ, L. BELOVA, V. STRÖM, L. A. BERGLUND, O. IKKALA, J. NOGUÉS, and U. W. GEDDE. Making Flexible Magnetic Aerogels and Stiff Magnetic Nanopaper Using Cellulose Nanofibrils as Templates. *Nature Nanotechnology* **2010**, *5*, 584–8.

[127] A. J. SVAGAN, M. A. S. A. SAMIR, and L. A. BERGLUND. Biomimetic Foams of High Mechanical Performance Based on Nanostructured Cell Walls Reinforced by Native Cellulose Nanofibrils. *Advanced Materials* **2008**, *20*, 1263–1269.

[128] H. SEHAQUI, M. SALAJKOVÁ, Q. ZHOU, and L. A. BERGLUND. Mechanical Performance Tailoring of Tough Ultra-High Porosity Foams Prepared from Cellulose I Nanofiber Suspensions. *Soft Matter* **2010**, *6*, 1824–1832.

[129] M. KETTUNEN, R. J. SILVENNOINEN, N. HOUBENOV, A. NYKÄNEN, J. RUOKOLAINEN, J. SAINIO, V. PORE, M. KEMELL, M. ANKERFORS, T. LINDSTRÖM, M. RITALA, R. H. A. RAS, and O. IKKALA. Photoswitchable Superabsorbency Based on Nanocellulose Aerogels. *Advanced Functional Materials* **2011**, *21*, 510–517.

[130] J. MALM, E. SAHRAMO, M. KARPPINEN, and R. H. A. RAS. Photo-Controlled Wettability Switching by Conformal Coating of Nanoscale Topographies with Ultrathin Oxide Films. *Chemistry of Materials* **2010**, *22*, 3349–3352.

[131] V. KEKKONEN, A. HAKOLA, T. KAJAVA, E. SAHRAMO, J. MALM, M. KARPPINEN, and R. H. A. RAS. Self-Erasing and Rewritable Wettability Patterns on ZnO Thin Films. *Applied Physics Letters* **2010**, *97*, 044 102.

[132] D. K. ROVETI. Choosing a Humidity Sensor: A Review of Three Technologies. *Sensors Magazine* **2001**, .

[133] L. YANG, S. LUO, Q. CAI, and S. YAO. A Review on TiO_2 Nanotube Arrays: Fabrication, Properties, and Sensing Applications. *Chinese Science Bulletin* **2010**, *55*, 331–338.

[134] N. S. RAMGIR, Y. YANG, and M. ZACHARIAS. Nanowire-Based Sensors. *Small* **2010**, *6*, 1705–22.

[135] Y. Zhang, W. Fu, H. Yang, Q. Qi, Y. Zeng, T. Zhang, R. Ge, and G. Zou. Synthesis and Characterization of TiO_2 Nanotubes for Humidity Sensing. *Applied Surface Science* **2008**, *254*, 5545–5547.

[136] J. J. Steele, M. T. Taschuk, and M. J. Brett. Response Time of Nanostructured Relative Humidity Sensors. *Sensors and Actuators B: Chemical* **2009**, *140*, 610–615.

[137] Q. Wang, Y. Z. Pan, S. S. Huang, S. T. Ren, P. Li, and J. J. Li. Resistive and Capacitive Response of Nitrogen-Doped TiO_2 Nanotubes Film. *Nanotechnology* **2011**, *22*, 025 501.

[138] Vaisala.fi. *HMT330 Series Datasheet*. `http://www.vaisala.fi/Vaisala Documents/Brochures and Datasheets/HMT330-Series-Datasheet-B210951EN-D-LoRes.pdf` (accessed 26.4.2013)

[139] A. B. Nordvik, J. L. Simmons, K. R. Bitting, A. Lewis, and T. Strøm-Kristiansen. Oil and Water Separation in Marine Oil Spill Clean-up Operations. *Spill Science & Technology Bulletin* **1996**, *3*, 107–122.

[140] B. Graham, W. K. Reilly, F. Beinecke, D. F. Boesch, T. D. Garcia, C. A. Murray, and F. Ulmer. Deep Water: The Gulf Oil Disaster and the Future of Offshore Drilling. Technical report, National Commission on the BP Deepwater Horizon Oil Spill and Offshore Drilling **2011**.

[141] H. Rousi and H. Kankaanpää, editors. Itämerellä tapahtuvien öljyvahinkojen ekologiset seuraukset. Technical report, Suomen ympäristökeskus **2012**.

[142] H.-M. Choi and R. M. Cloud. Natural Sorbents in Oil Spill Cleanup. *Environmental Science & Technology* **1992**, *26*, 772–776.

[143] Q. F. Wei, R. R. Mather, A. F. Fotheringham, and R. D. Yang. Evaluation of Nonwoven Polypropylene Oil Sorbents in Marine Oil-Spill Recovery. *Marine Pollution Bulletin* **2003**, *46*, 780–783.

[144] J. G. Reynolds, P. R. Coronado, and L. W. Hrubesh. Hydrophobic Aerogels for Oil-Spill Clean Up - Synthesis and Characterization. *Journal of Non-Crystalline Solids* **2001**, *292*, 127–137.

[145] A. V. Rao, N. D. Hegde, and H. Hirashima. Absorption and Desorption of Organic Liquids in Elastic Superhydrophobic Silica Aerogels. *Journal of Colloid and Interface Science* **2007**, *305*, 124–132.

[146] J. L. Gurav, A. V. Rao, D. Y. Nadargi, and H.-H. Park. Ambient Pressure Dried TEOS-Based Silica Aerogels: Good Absorbents of Organic Liquids. *Journal of Materials Science* **2009**, *45*, 503–510.

[147] X. Gui, J. Wei, K. Wang, A. Cao, H. Zhu, Y. Jia, Q. Shu, and D. Wu. Carbon Nanotube Sponges. *Advanced Materials* **2010**, *22*, 617–621.

[148] F. C. Moura and R. M. Lago. Catalytic Growth of Carbon Nanotubes and Nanofibers on Vermiculite to Produce Floatable Hydrophobic "Nanosponges" for Oil Spill Remediation. *Applied Catalysis B: Environmental* **2009**, *90*, 436–440.

Errata

Publication I

On page 3858, $\cos\theta_r - \cos\theta_a$ was incorrectly denoted as *work of adhesion*. The formula is correct, yet the appropriate description would be the force required to move a drop on a surface.

Aalto-DD 116/2013

ISBN 978-952-60-5259-5
ISBN 978-952-60-5260-1 (pdf)
ISSN-L 1799-4934
ISSN 1799-4934
ISSN 1799-4942 (pdf)

Aalto University
School of Science
Department of Applied Physics
www.aalto.fi

BUSINESS +
ECONOMY

ART +
DESIGN +
ARCHITECTURE

SCIENCE +
TECHNOLOGY

CROSSOVER

DOCTORAL
DISSERTATIONS